VRIJE
UNIVERSITEIT
BRUSSEL

Graduation thesis submitted in partial fulfillment of the requirements for the degree of Master in Physics and Astronomy

STUDY OF ENVIRONMENTAL RADIATION WITH PLASTIC SCINTILLATORS

Fien Dewit

May 31, 2024

Promotors: Prof. Dr. Didar Dobur and Prof. Dr. Steven Lowette
Supervisor: Dr. Kirill Skovpen

Sciences and Bioengineering Sciences

Acknowledgement

I would like to thank Prof. Didar Dobur for welcoming me to the team at the University of Ghent and for providing me with the incredible opportunity to work on my thesis topic and internship in particle physics. Despite having studied at the VUB for some time, I always felt at ease coming to UGent.
Furthermore, I owe many thanks to my supervisor Kirill. He consistently guided me back on track when I could not see the outcome or was overwhelmed by confusion. Throughout the academic year, he answered numerous questions, helped me develop a critical eye for results, and encouraged me during the slow initial stages. You were a great supervisor.

I would also like to thank my boyfriend, Fred, for his support during the whole journey of the thesis. You were a pillar to lean on whenever I needed you.

Summary

Natural radiation surrounds us in everyday life. This natural source consists of a variety of particles with a wide variety of energies, making it an interesting source for research in the context of particle physics.

Several retired detector parts became available for use during this thesis. These included plastic scintillators and neutron screens from the SoLi∂ experiment. However, before immediately starting with these detectors and risking getting lost in this extensive source of particles, a study was first conducted into how exactly these detectors respond to environmental radiation.

Simulations with Geant4 are an excellent method to gain better insight into the operation of the components. It soon became clear that with a single scintillator, almost all charged particles can be measured across a wide energy range. Adding a neutron screen allowed for the detection of neutrons as well.

With only a cube and neutron screen, it became apparent that drawing conclusions about which particle passed through the detector would be a challenging task. Therefore the horizon was broadened to explore detector constructions to gain additional information on the environmental radiation.

Adding a moderator helps to slow down neutrons and establishes a lower limit on the energy of detectable particles.

Using a sampling calorimeter setup, the passage of a particle can provide additional information since particles shower in the detector. While simulations helped to gain a better insight into electromagnetic showers, no definitive conclusion could be drawn for hadron showers.

Several cubes stacked on top of each other can provide information about the direction from which the particle came. It found that the use of Tyvek is recommended.

Finally, it was briefly discussed how several layers of scintillators can determine the lifetime of a muon.

Contents

Introduction

At the heart of particle physics lies the understanding of nature. In nature, everything is built up of particles that interact with each other. They follow certain laws strictly by the book. The quest to uncover these laws of nature are has kept humankind occupied for centuries [1].

The Standard Model of particle physics [2] is the most commonly used theory that unifies the fundamental particles and three of the fundamental forces in one framework. This theory was written down in the early 1970s and explains nearly all experimental results [2].

The fundamental particles of the Standard Model are regarded as the building blocks of nature. Atoms consist of electrons, protons and neutrons. Electrons ($e-$) fall under the category of leptons and, together with the electron neutrino (ν_e), form the first generation. The second lepton generation includes the muon (μ) and muon neutrino (ν_μ). The tau (τ) and the tau neutrino (ν_τ) constitute the third generation. The electron, muon and tau lepton all have a charge equal to $-e$. These particles interact via electromagnetic and weak interactions. Their accompanying particles, the neutrinos, are chargeless and thus only interact via weak interaction. Within the nucleus of an atom, the protons and neutrons are composed of up (u) and down (d) quarks. Up quarks have a charge of $+2/3e$ and down quarks of $-1/3e$. Together, they form the first generation of quarks. The second quark generation consists of charm (c) and strange (s) quarks, followed by the third generation: top (t) and bottom (b) quarks. All these particles interact with each other via the weak and strong force and, since they have a charge, they can also interact via the electromagnetic force. Additionally, quarks never appear alone but are always bound together to form a larger particle. For example, two up quarks and one down quark together form a proton. Other combinations of quarks give rise to different particles. Three quarks that bond fall under the category of hadrons, which include protons (p), neutrons (n), etc. If only two quarks bond, they are called mesons. Examples of this are pions (π), kaons (K), etc[1] [2].

A comprehensive illustration of all the Standard Model particles is given in figure 1. The figure also includes the boson particles. All the previously described interactions occur via the exchange of bosons. The gluon (g) mediates strong force interaction, the photon (γ) mediates electromagnetic interaction and the W and Z bosons mediate the weak interaction.

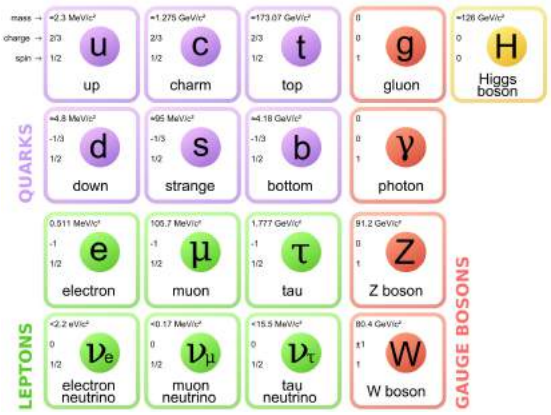

Figure 1: Standard Model view of the fundamental particles.

The most recently discovered particle of the Standard Model was the Higgs boson in 2012. This boson is a manifestation of the Brout-Englert-Higgs mechanism, which contributes to our understanding of the origin of mass of subatomic particles.

Even though this zoo of particles seems somewhat exotic they surround us all the time. On Earth, all the matter is built up of electrons, protons and neutrons. But even second-generation particles like muons constantly reach us via cosmic rays. Since our daily environment is so richly filled with these particles, it is interesting to examine them with some retired detector parts from the SoLi∂ experiment. This thesis will dig deeper into the understanding of scintillators and neutron screens and explore their horizon of possibilities.

In the first chapter, we will discuss environmental radiation. We will outline where environmental radiation is high, what causes it, and its composition. The next chapter examines the detector parts used to observe these particles by delving into the working principles of scintillators, neutron screens, wavelength-shifting fibers and silicon photomultipliers. A very useful way to gain more insight into how these particles react in the detectors can be achieved using computer simulations. The toolkit used in this thesis is discussed in Chapter 3. The obtained simulation results are then further validated and discussed in the subsequent chapter. Afterward, the detector components' horizon of possibilities is explored in Chapter 5. Various applications with the detector parts are considered here. Some roads regarding applications with the detector parts are explored. Finally, a conclusion is presented to tie everything together neatly.

Chapter 1

Natural Radiation

Naturally, the human body is exposed to an average of 4 to 5 mSv per year in Belgium[3]. A series of sources lies at the origin of this exposure. Figure 1.1 sketches some of them.

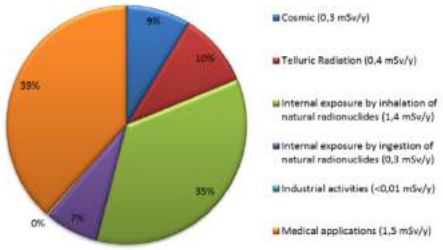

Figure 1.1: Average exposure to ionizing radiation in Belgium was 4 mSv per year in 2015 [3].

Radioactivity is mainly categorized by two origins: a natural origin and an artificial origin [3]. As one can see, the most common source is exposure by medical applications. This contains radiological imaging and other treatments. A computed tomography scan is performed only a few times in a human's lifetime, yet the used doses are rather high. A source of much lower doses but to which people are exposed on a daily basis is cosmic radiation and the presence of natural radioactive sources in their surroundings. It is prescripted by law that the population of Belgium may not receive a higher dose of ionizing radiation than 1 mSv per year [3]. This does not take into account background radiation such as cosmic rays, the radiation of the soil and subsoil or the radiation used for medical purposes. This thesis will elaborate further on the natural origins of radioactivity.

1.1 Cosmic Rays

In 1912, during an air balloon flight, Victor Hess discovered an increase in ionizing radiation with altitude. From this, he wrote "The results of the present observations seem to be most readily explained by the assumption that a radiation of very high penetrating power enters our atmosphere from above ... Since I found a reduction ... neither by night nor at a solar eclipse, one can hardly consider the Sun as the origin."[1] [4].
From this point, numerous experiments have been conducted to understand the nature of the so-called cosmic rays. The term "cosmic rays" encompasses not only gamma rays but all particles coming from outer space that travel through the Earth's atmosphere.

1.1.1 In space

Cosmic rays are elementary particles and atomic nuclei that reach the Earth from outer space. The majority of the cosmic ray particles are protons (about 90%) and alpha particles (nearly 9%)[6]. The remaining particles are electrons and nuclei heavier than helium[6]. The direction of cosmic rays does not reveal information about their place of origin since the electrically charged particles are deflected by magnetic fields along their journey. Nevertheless, their very high energies (ranging from 10^8 to 10^{20} eV) indicate that they are produced by high-energy phenomena in space[7].

- Cosmic rays are emitted in bursts when the Sun flares. This occurs when a large amount of energy that is stored within the magnetic field suddenly gets released [6]. These outbursts, also emit numerous solar particles, which are accelerated to high energies by the shock waves from these outbursts[7].

- The majority of cosmic rays originate from outside the solar system, predominantly from supernovae. A supernova is the spectacular explosion of a star at the end of its life. It induces relativistic particles via the shock wave formed in the expanding supernova remnants.[7].

- Some galaxies in the universe show intense light from their nuclei. These are known as active galactic nuclei (AGN) and can emit much more energy than a normal galaxy. Mechanisms similar to supernovae accelerate particles to very high energies via shock waves.

The collection of radiation from these sources propagating through space is called the *primary cosmic rays*. The primary cosmic ray fluxes can be described by a power law. Since the goal of this thesis is to focus on the cosmic rays at ground level, this topic

[1] Citation extracted from a translation of the original paper by Hess, taken from *Cosmic Rays: The Commonwealth and International Library: Selected Readings in Physics* by A.M. Hillas [5]

will not be discussed further in detail.

1.1.2 On Earth

As primary cosmic rays reach the Earth, they interact with the atmosphere, hitting air molecules and producing "secondary cosmic rays" [10]. The reaction products will continue to travel through the atmosphere, collide with other particles and create a cascade of reactions, known as a "shower".
When protons interact with atmospheric molecules, they cause so-called "proton shower" (see figure 1.2). These showers produce various particles, including pions via strong interactions. Pions (π^+, π^0, π^-) are classified as mesons since they consist of a quark and an antiquark. They have a mass of approximately 140 MeV/c^2 and a lifetime of the order of 26 ns. This means that pions will rapidly decay into other particles. The charged pions in the showers, tend to decay into muons via weak interaction processes:

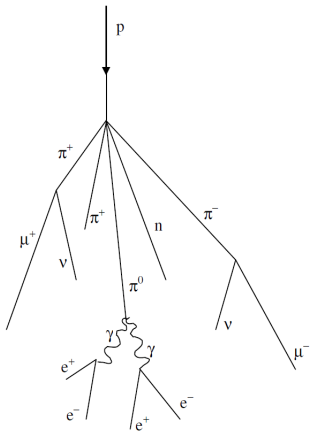

Figure 1.2: Visualisation of proton shower inside the Earth's atmosphere[8].

$$\pi^+ \rightarrow \mu^+ + \nu_\mu$$
$$\pi^- \rightarrow \mu^- + \nu_\mu$$

Although it is with a lower cross-section, protons can also decay into kaons, which further decay into muons.

Since muons have a long enough lifetime to reach the Earth's surface, we can observe muons as the most abundant high-energy particle of the secondary cosmic rays at ground level. An estimated spectrum of cosmic rays at ground level can be seen in figure 1.3. Because primary cosmic rays are composed of charged particles, low energetic cosmic rays can be deflected by the Earth's magnetic field towards the North or South Pole. This is why the cosmic ray spectra at ground level depend on latitude. There is also a dependency on longitude and altitude[9][12]. The longitudinal dependency lies in the East-West effect [11], which indicates that positively charged particles tend to be deflected East and negatively charged particles West because of the Earth's magnetic field. Altitude also plays a role since, at higher altitudes, the constituents of the particles in the shower can differ from those observed at ground level.
This thesis will focus on the particle sources that are most easily accessible: radiation at ground level. Measuring the cosmic ray fluxes at ground level is a challenging task

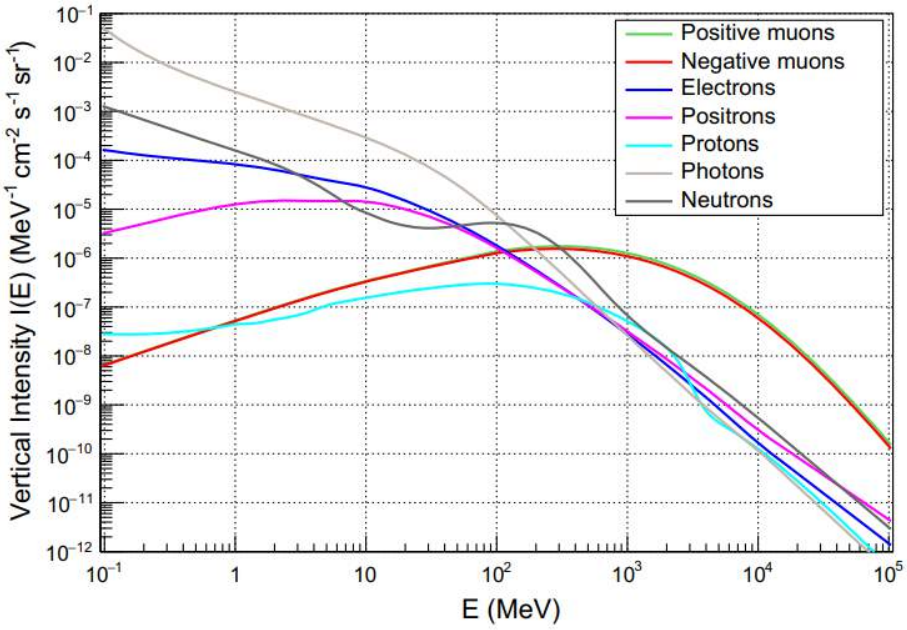

Figure 1.3: Differential vertical intensity of secondary cosmic rays at ground level as a function of the energy at (45° N 15° E) Earth Position and on August 1, 2018, computed using the PARMA model as described in the text. The contributions from the various particle species are plotted[13]

to achieve as one has to map a wide range of energies for several types of particles. Some examples of ground-level experiments in this domain are KASCADE [15], LOFAR [16], and the Pierre Auger Project [17]. If a certain particle's flux rate is not high in a specific energy range, it requires a very long time to obtain enough data. Therefore a more commonly used approach to sketch the cosmic ray fluxes at ground level is through estimations by Monte Carlo simulations. An example of such a simulation can be seen in figure 1.3. Here the so-called PARMA model [13] is used to obtain the ground-level cosmic ray spectrum at 45° N 15° E.
As can be seen from figure 1.3, the muons are the most abundant for particle energies above a few hundred MeV. This is because they are widely produced in proton showers and their lifetime is much longer than that of other particles (pions, kaons, etc.) in these showers. The plot also distinguishes between positive muons μ^+ and negative muons μ^-. A slightly higher positive muon flux is an interesting detail. This smaller excess in comparison with the negative muons originates from the cosmic showers that are mostly caused by positively charged protons. The laws of conservation of charge predict that positively charged particles will be more abundant than negatively charged particles.

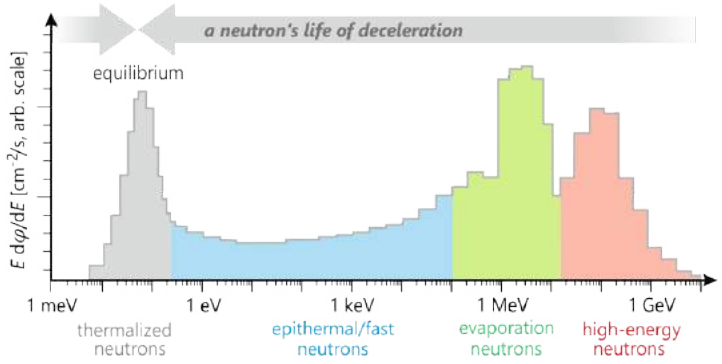

Figure 1.4: Neutron spectrum at ground level[14]

At lower energies, neutrons have the highest flux rate. Most of the neutrons are products of primary and secondary cosmic rays reactions with nitrogen and oxygen nuclei [19]. The produced high-energy neutrons are continuously slowed down by numerous elastic and inelastic collisions with nuclei in the atmosphere. The neutron spectrum at ground level can generally be divided into three regions: high-energy neutrons (above 100 MeV), evaporated neutrons (around 1 MeV), and low-energy neutrons in thermal equilibrium with its environment (less than 0.5 eV). The epithermal/fast neutron region (0.5 eV to 100 keV) in figure 1.4 has the property of being sensitive to energy loss in collisions with hydrogen[14]. Note that the spectrum in figure 1.4 not only includes cosmic ray neutrons but also neutrons released by the creation of cosmogenic nuclides or radioactive decay. More on this will be discussed in the next sections.

1.1.3 Cosmogenics

Cosmic rays evolving through the atmosphere or the upper layer of Earth's surface can cause nuclear reactions which create *cosmogenic nuclides*[18]. Several factors may trigger variations in these cosmogenic nuclei formations. Genarally, these are the same factors that cause variations in the secondary cosmic ray formation. The fluctuation of cosmic rays is correlated with solar activity[20] but also with variations in the Earth's geomagnetic field that influences the partial amount of cosmic rays that get screened and modulated by the Earth's magnetic field [21]. Besides these effects, the intensity of the cosmic rays is strongly tied together with the altitude [18] [22]. All these effects on the cosmic rays also cause variations in the production rates of cosmogenic radionuclides.
The formation of cosmogenics is strongly dependent on the nucleon flux, the neutron-to-proton ratio and the available energies. The production of radionuclides at sea level is mainly dominated by thermal neutrons since particles like protons are absorbed in the atmosphere. But at high altitudes, where the cosmic ray flux is larger, the particles have higher energies and the creation by proton cannot be neglected [23].

After primary cosmic rays reach the Earth, and secondary cosmic rays are produced in showers in the atmosphere, the radionuclides can be formed by nucleonic reactions in the atmosphere or at the Earth's surface [24]. Spallation, neutron capture or muon capture fall under this category.
A spallation reaction is a violent reaction that appears when a highly energetic nucleon collides with a target nucleus. Multiple particles such as protons, neutrons, and clusters are released in spallation reactions. These accelerated particles that are produced cause secondary reactions that can strike other atmospheric nuclei along their path and cause further spallation reactions. The cascade of creation of cosmogenic nuclides and high-energy neutrons goes on successively until the particles' energies are too low to further undergo spallation reactions when colliding with other particles.
Even though spallation reactions are by far the most common way to produce cosmogenic radionuclides in the atmosphere, induced fission, fragmentation, and capture reactions may not be left out as they are very important for the formation of some nuclei [23]. Most of the cosmogenic nuclides are formed in the atmosphere and some in soils and rocks. Slow muon and neutron capture as processes to create cosmogenic radionuclides are the most common processes to form cosmogenic nuclei at the Earth's surface. These kinds of cosmogenic nuclei are often called *terrestrial cosmogenic radionuclides* [18][26]. At the top few centimeters of a rock, the cosmic ray intensity gets attenuated. This is the place where the terrestrial cosmogenic radionuclides are formed[26].
The most commonly occurring cosmogenic radionuclides are ^{7,10}Be, ^{32,33}P, ^{22}Na, ^{35}S, ^{39}Cl, ^{26}Al, ^{14}C and ^{3}H. Table 1.1 lists these isotopes together with the creation mode and the half-life of the nuclide. Some of these isotopes are stable, others are radioactive.

1.2 Natural occurring radioactive sources

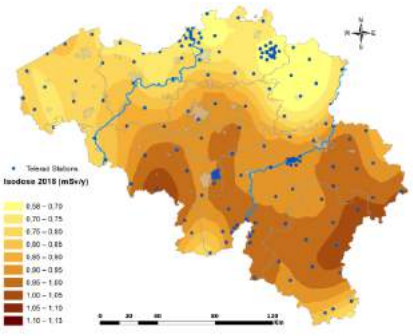

(a) Natural background radiation due to gamma radioactivity to which a certain location is subjected.

(b) Map with naturally occurring soils in Belgium.

The Federal Agency for Nuclear Control of Belgium compiled a map that shows the

Isotope	Formation mode	Half-life
^{3}H (triton t)	^{14}N(n,^{12}C)t	12.3 years
^{7}Be	Spallation (N and O)	53.2 days
^{10}Be	Spallation (N and O)	1 387 000 years
^{14}C	^{14}N(n,p)^{14}C	5730 years
^{22}Na	Spallation (Ar)	2.6 years
^{26}Al	Spallation (Ar)	717 000 years
^{32}P	Spallation (Ar)	14.3 days
^{33}P	Spallation (Ar)	25.3 days
^{35}S	Spallation (Ar)	87.5 days
^{39}Cl	^{40}Ar (n,np)^{39}Cl and spallation (Ar)	56 minutes

Table 1.1: Table of properties of the most prominent cosmogenic nuclides

external background exposure dose across Belgium. This can be seen in figure 1.5a. The blue dots represent the measuring stations (the TELERAD stations) installed by the FANC across the country. Based on measurements and mathematical extrapolation, different values were grouped under the same color, indicating different zones where the measurements fell within the same category. The values of the different categories are displayed in mSv and represent the natural background radiation due to gamma radioactivity. In this way, one can see what the exposure is to which an area is subjected[3]. Figure 1.5a indicates that overall Flanders is subjected to about 0.8 - 0.9 mSv/years. In Wallonia, this is about 1.0 to 1.1 mSv/year, more particularly in the Ardennes [3].
This map can be compared with a map of the occurring soils in Belgium. Generally, the regions with high doses are territories with old terrains made up of rocks such as schist, chalkstone, psammite and mixed sands with chalk etc. This is predominantly for Belgium in the Ardennes and the Condroz area. The lower doses in Flanders appear where the soil is mostly made up of sedimentary terrains such as sand, alluvium and clay [3].

All natural occurring radioactive sources that cause the exposure that is measured and summarized in the previous plot, can be grouped as follows[26]:

- Radionuclides that have been present since the formation of the Earth. These have a very long lifetime and were probably synthesized by nuclear reactions in stellar explosions even before the formation of our solar system. The isotopes in this category occur throughout our environment, mainly in soils and rocks. The main isotopes here are ^{40}K, ^{238}U, ^{232}Th, ^{235}U, etc.

- The disintegration of the group of isotopes just mentioned is usually accompanied by long decay chains, especially from ^{235,238}U and ^{232}Th. A lot of neutrons, protons, alpha rays and gamma rays are in this way released. Since neutrons can travel a relatively long distance through matter, they end up with low energies in the atmosphere. The radionuclides produced in these chains can be grouped. The most prominent isotopes here are ^{228,230}Th and ^{220,222} Rn.

- The radionuclides (cosmogenic nuclides) mentioned in section 2.1.3, which are formed by nuclear reactions of cosmic rays with the atmosphere, soil and rocks form the last group.

An overview of some properties of these isotopes can be seen in table 1.2.

Isotope	Half-life	Decay mode	Decay product
^{40}K	$1,248 \times 10^9$ years	β^+, β^-	^{40}Ar,^{40}Ca
^{220}Rn	55.6 seconds	α	^{216}Po
^{222}Rn	3.82 days	α	^{218}Po
^{228}Th	1.92 years	α	^{224}Ra
^{230}Th	75 400 years	α	^{226}Ra
^{232}Th	1.405×10^{10} years	α	^{228}Ra
^{235}U	7.04×10^8 years	α	^{231}Th
^{238}U	4.468×10^9 years	α	^{234}Th

Table 1.2: Table of properties natural occurring radioactive isotopes.

1.3 Summary

In everyday life, people are exposed to various types of radiation. Cosmic radiation showers produce high-energy muons and lower-energy neutrons and electrons that constantly bombard us. Occasionally, cosmic rays interact with the atmosphere, causing nuclear reactions that create isotopes known as cosmogenic nuclides. These rays can also interact with the soil, contributing to our radiation exposure. When radionuclides are present in the soil for extended periods, they may undergo decay. This long decay

process often results in the production of numerous neutrons, protons, alpha particles, and photons.
For a physicist, these abundant and free sources of particles with different energy levels are fascinating. These sources will be utilized further in this thesis.

Chapter 2

Detector components and materials

Before certain setups can be made with the retired detector parts from the SoLi∂ experiment, it is interesting to have a better understanding of how they work. In the following, the detection of charged particles with plastic scintillators and the detection of neutrons with the neutron screens are discussed. This is followed by a brief discussion of the main interaction mechanisms for photons. The wavelengthshifting fiber that guides the light from the inside of the scintillator towards the Silicon Photomultiplier (SiPM) will also be shortly seen here. This chapter follows some descriptions of interactions and working principles mentioned in *Radiation Detection and Measurement* by G.F. Knoll [27].

2.1 Charged Particle Detection

Various detector systems are available to record the passage of charged particles. This section will only focus on the detector that is relevant to this thesis: the scintillator.

2.1.1 Scintillators

Two types of scintillators are used in this thesis. One is polyvinyl toluene (PVT) cut up in cubes of 5 cm $\times$ 5 cm $\times$ 5 cm, which is an organic scintillator. The other one is ZnS(Ag) used together with ^{6}LiF to capture thermal neutrons[28]. The latter one is a loaded plastic scintillator.

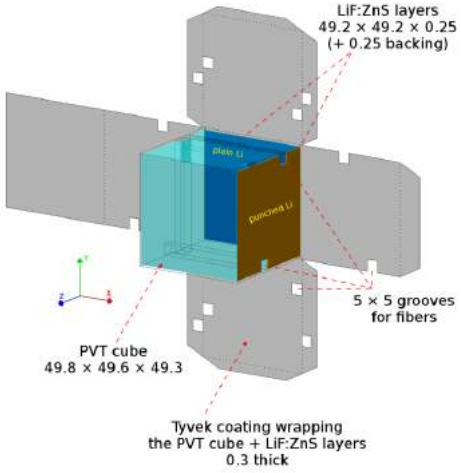

Figure 2.1: Retired SoLi∂ parts consisting of a plastic scintillator cube, a LiF:ZnS neutron screen wrapped in Tyvek. Wavelength shifting fibers (WLS) through the cube and holes of the tyvek are guiding the scintillation light to the SiPM [47].

2.1.1.1 Scintillation mechanism in organic scintillators

Fluorescence is defined as the spontaneous emission of radiation that occurs during the irradiation of a certain substance by electromagnetic radiation. The electromagnetic radiation excites an atom and when the atom de-excites again, it goes along with the emission of a photon. In organic materials, the fluorescent process originates from the transition between energy levels in a single molecule. This emitted radiation is independent of the physical state of the scintillator material. This is in contrast with inorganic scintillators, which need a regularly arranged crystal lattice for the scintillation process to happen. In organic scintillators, the atoms will bind to each other to form a molecule. The Molecular Orbital (MO) model is a theory that describes the electron structures of molecules by making use of quantum mechanics. It describes the states of bonding electrons by approximating them as linear combinations of atomic orbitals (LCAO). As we will need the electron structure to further explain the principle of a scintillator, an example is shown in figure 2.2. Because this is not the core of the thesis, we will not dig deeper into the reasoning for this structure but just show the MO model result of two p-orbitals combining into a so-called π-electron structure. Figure 2.2 is divided into singlet states and triplet states. Singlet states have spin 0 and are written down as S_0, S_1, S_2,... while triplet states have spin 1 and are described by T_0, T_1, T_2, ... In organic scintillators, the distance between S_0 and S_1 is around 3 or 4 eV while the distance between higher states is typically somewhat smaller. One can notice that each of these states is divided into several energy levels with smaller spacing between them. These represent the vibrational states of the molecule. To mark these energy levels, a second number is added to the subscription. The S_{00} thus describes the lowest vibrational state of the ground level. Since the spacing between the vibrational

states (typically around 0.15 eV) is large compared to their average thermal energy (0.025 eV), nearly all molecules are in the S_{00} state at room temperature.
An upward-pointing arrow in the figure stands for the absorbed energy by a molecule. The system goes from a lower energy state to a higher energy state. This absorption is caused, in the case of a scintillator, by the kinetic energy of a charged particle passing by. Through radiationless conversion, the higher excited singlet electronic states de-excite fast (order of ps) to the S_1 states. Any state with an excess of vibrational energy (such as S_{11} or S_{12}) is not in thermal equilibrium with its neighbors and thus quickly loses its excess of vibrational energy. The net effect of a passing charged particle through the scintillator will thus cause excitation processes that produce, after a very short time, several excited molecules that are situated in the S_{10} state. When a transition from the S_{10} state to any vibrational state of the electronic ground state occurs, a photon is emitted. This scintillation light is also known as *prompt fluorescent light* Such a transition is marked as a downward arrow in the figure. With τ the decay time of the S_{10} level with fluorescent light, the intensity of the prompt fluorescence at a time t after excitation is written as

$$I = I_0 e^{-t/\tau} \tag{2.1}$$

This τ is of orders of a few nanoseconds for most organic scintillators. This prompt scintillation light happens relatively fast.

Excited singlet states can via an "intersystem crossing" transition be converted into triplet states. In comparison with the singlet state S_1 is the lifetime of the triplet state T_1 typically much longer, namely of order $10^{-3}s$. This means that radiation from de-excitation of the T_1 to S_0 state will be observed with a delay in comparison with prompt fluorescent light. Since the wavelength of the delayed photon is longer because the T_1 energy level lies below the S_1 energy level, this radiation is called *phosphorescence*. Molecules in the $T1$ state can via thermal excitation also go back to the S_1 state. The decay from the S_1 state then results back in normal, but yet delayed fluorescence.
The reason why organic scintillators are transparent for their own fluorescent emission light can also be seen in figure 2.2. Since the length of the downward arrows is shorter than the length of the upward arrows, absorption of fluorescent emission light will not occur. In other words, the energy of the photons that are emitted is lower than the required energy to cause excitation of an absorber atom. The only exception here is the $S_{10} - S_{00}$ transition. Hence there will only be little overlap between the absorption and emission spectra of organic scintillators. This overlap is often called *Stokes shift* and an example of this little self-absorption can be seen in figure 2.3.

In addition to low self-absorption, it is also preferred that the *scintillation efficiency* is as high as possible. The scintillation efficiency is defined as the fraction of the incident particle energy that is converted into optical light [27]. Unfortunately, various de-excitation modes are available in which the excitation energy is converted radiationless into heat. All these radiationless processes together are named *quenching*.

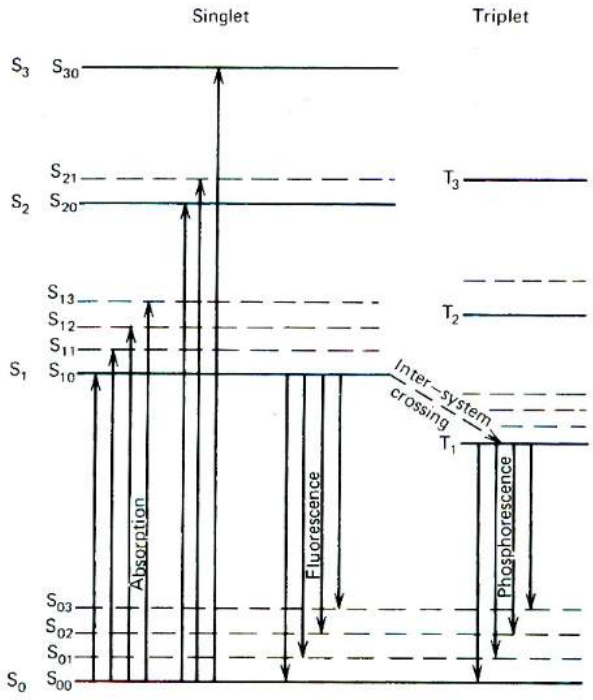

Figure 2.2: Energy levels of an organic molecule with π-electron structure.[27]

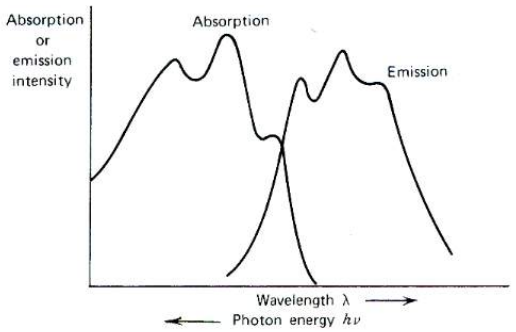

Figure 2.3: The optical absorption and emission spectra for a typical organic scintillator with the level structure shown in figure 2.2.[27]

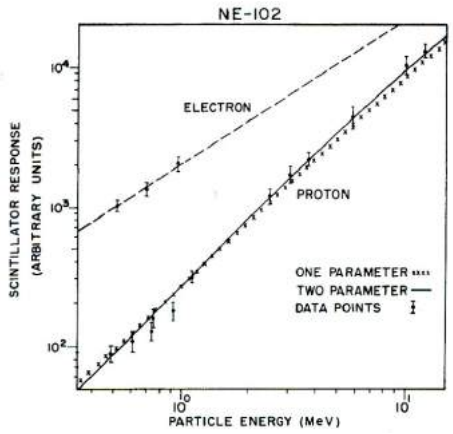

Figure 2.4: The scintillation light yield for a common plastic scintillator (NE 102) when excited by electrons and protons.[27]

2.1.1.2 Light output of scintillators

The fraction of the kinetic energy of the incoming particle that is converted into fluorescent light is dependent on both the kind of particle and its energy. There exist however some cases where the part the particle energy and the scintillation efficiency are independent from each other. This results in a linear dependence of light yield with the particle's initial energy.

The response to electrons is for lots of commercially available plastic scintillators linear for particle energies above about 125 keV [27]. For heavier particles such as protons or alpha particles at equivalent energies, the response is always lower than for electrons and is even non-linear at high initial energies. Figure 2.4 shows the scintillation response for a typical plastic scintillator to illustrate the situation. The difference between the curves is smaller for higher initial energies, however the proton response is still smaller than the electron response.

According to G.F. Knoll, the response of organic scintillators on charged particles can best be described by the relation between the fluorescence emission per unit of path length dL/dx and the specific energy loss of the charged particle dE/dx. Together with the normal scintillation efficiency S, this relation becomes:

$$\frac{dL}{dx} = S\frac{dE}{dx} \tag{2.2}$$

The further assumption is now made that a particle introduces a high ionization density along its path that gives rise to quenching due to damaged molecules. Due to this quenching, the scintillation efficiency decreases. This assumption was suggested by British physicist John B. Birks. If the density of damaged molecules along a particle's path is proportional to the ionization density, then this can be written down as $B(dE/dx)$. In this expression, B represents a proportionality factor. Birks then

supposes that not all of these damaged molecules will lead to quenching, but only a fraction k. Bringing into account these assumptions about quenching then modifies equation 2.2 to

$$\frac{dL}{dx} = \frac{S\frac{dE}{dx}}{1 + kB\frac{dE}{dx}} \tag{2.3}$$

This equation is also known as *Birks' formula*.

2.1.1.3 Time response of scintillators

When a particle passes through a scintillator, its interaction with the material will lead to a very fast population of the luminescent state. Although this happens almost instantaneously, the time to populate the luminescent state must be taken into account when considering the time profile of the light pulse. A slower component must also be taken into account to describe the decay from this luminescent state by prompt fluorescence, phosphorescence and delayed fluorescence. The time to populate the states is usually around 1 ns. Since the decay time of these levels is only 3 to 4 times longer in fast scintillators, is it crucial to take into account this finite rise time of the pulse. If we assume that the time to populate the optical levels also happens exponentially, then the time profile for the light pulse can be described by

$$I = I_0 \, (e^{-t/\tau} - e^{-t/\tau_1}) \tag{2.4}$$

with τ_1 the time constant that describes the population of the optical levels and τ the time constant that describes their decay [27]. In some cases, it is better to describe the population part of the formula by a Gaussian function $f(t)$ with standard deviation σ_{ET}. The overall light as a function of time can then be described by

$$\frac{I}{I_0} = f(t) \, e^{-t/\tau} \tag{2.5}$$

For very fast scintillators, note that other effects can influence the observed time response. Among these is the finite time of flight of the photons from the point of scintillation to the photomultiplier.

2.1.1.4 Pulse shape discrimination

In the majority of the organic scintillators is most of the scintillation light represented by prompt fluorescence. The longer-lived component that is observed is represented by delayed fluorescence. As an alternative to the previously discussed equation 2.4, the decay component can be represented by the sum of the fast component (prompt fluorescence) and a slow component (delayed fluorescence). The prompt decay time is only a few nanoseconds while the slow component is typically a few hundred nanoseconds. One would expect that the slow component is of little interest since most of the light is produced by the prompt component. However, there is one very interesting application:

the fraction of light that appears in the slow component is in most cases dependent on the type of particle that excited the medium. One can thus use this dependency to make a distinction between the different types of particles that deposit the same amount of energy in the scintillator. This process is called *pulse shape discrimination*. It is commonly applied to eliminate gamma-ray-induced events when organic scintillators are used as neutron detectors. An example of this can be seen in figure 2.5. While pulse discrimination remains a useful concept to consider, its implementation becomes challenging during cosmic ray observations due to varying light intensities across different energy ranges, where specific particles are more prevalent.

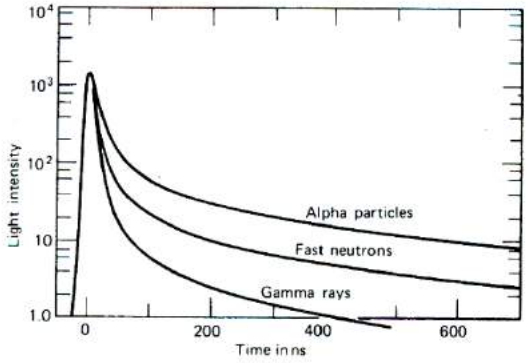

Figure 2.5: The time dependence of scintillation pulses in stilbene (equal intensity at time zero) when excited by radiation of different types. [27]

2.1.1.5 Specifics of the used scintillators in this thesis

Polyvinyltoluene (PVT) is the type of plastic that is used for the scintillators in this thesis. More specifically it is a general-purpose plastic scintillator of type EJ-200 and produced by ELJEN Technology[29]. Its has the size of a 5 cm $\times$5 cm $\times$5 cm cube. A property of this scintillator is that it emits 10 000 photons per MeV of deposited energy. The light of the produced photons is classified in the blue-violet wavelength band of the electromagnetic spectrum. The emitted light peaks at a wavelength of 425 nm. The choice of this PVT material is mainly motivated by the good light response and the linear energy response over a wide range of energies ranging from 100 keV to several MeV [46][45]. The scintillator has an excellent decay time of 2.1 ns [30].

The ^{6}LiF:ZnS(Ag) screen is a combination of a loaded plastic scintillator (ZnS(Ag)) together with ^{6}LiF for neutron detection. It is produced by SCINTACOR in the form of thin screens[31] that can be placed at the sides of the PVT scintillator cube. The decay time of this so-called neutron screen is around 10 microseconds. The neutron screens emit photons at a peak emission wavelength of 450 nm [48].

2.2 Neutral particle detection

The dominant energy loss mechanism of charged particles passing through matter is via interaction with the Coulomb force. Since neutral particles like photons and neutrons do not carry any electric charge, they have to interact via another force.
Neutrons can travel a relatively long distance through matter before interacting. When they do interact, this happens with a nucleus of the absorber material. The result of this interaction is that the neutron may disappear and be replaced by one or more secondary particles. Another option is for the neutron to scatter elastically with a nucleus so the neutron can change its direction or energy drastically. The produced secondary particles after a neutron interaction are almost always heavy charged particles. These originate either from neutron-induced nuclear reactions or they may be the nuclei of the absorbing material itself, which have gained energy as a result of neutron collisions. To observe the passage of a neutron, a material has to be added that easily interacts with the neutron and detects these secondary particles directly. This is why the scintillator cube has to be accompanied by a so-called "neutron screen". This neutron screen is made of LiF:ZnS and has a size of 49.2 mm $\times$ 49.2 mm $\times$ 0.25 mm.

2.2.1 Slow neutron detection

Neutrons with an energy below 0.5 eV are defined as slow neutrons. We will limit our discussion on slow neutrons to the detection with no attempt to be aware of their kinetic energy.
The passage of a slow neutron can be noticed when the slow neutron interacts with the absorber material in a nuclear reaction. In order to build efficient detectors with small dimensions, the cross-section for a nuclear reaction should be as high as possible. This is why the neutron screen is a ZnS scintillator material that is enriched with LiF.
The "Q-value" of the reaction is also of importance. This is defined as the amount of energy that is released during the nuclear reaction. The larger the Q-value is, the more energy can be given to the reaction products and the easier it will be to separate neutron signals from photon signals.
Some possibilities of common nuclear reactions with slow neutrons and heavy charges particles as products are:

$$\text{neutron + target nucleus} = \begin{cases} \text{recoil nucleus} \\ \text{proton} \\ \text{alpha particle} \\ \text{fission fragments} \end{cases}$$

The reaction does not give any information price on the kinetic energy of the slow neutron because the kinetic energy of the reaction products is only determined by the Q-value. The neutron screen that is used for this study involves ^{6}Li. So the reaction that appears in the neutron screen is

$$^6_3Li + ^1_0n \rightarrow ^3_1H + ^4_2\alpha \qquad \text{(Q-value = 4.78 MeV)}$$

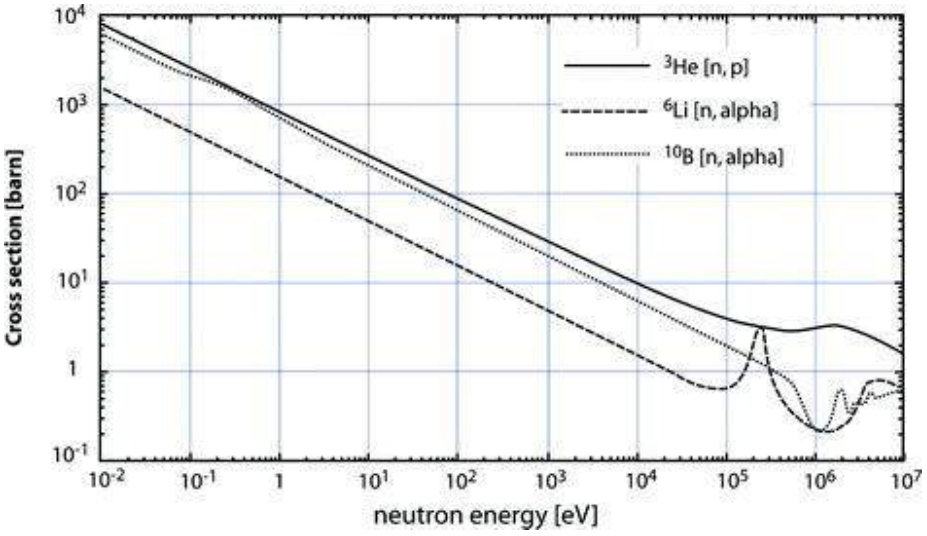

Figure 2.6: Cross-section as a function of the neutrons energy for ^{3}He, ^{6} Li and ^{10}B target nuclei reactions.[27]

This reaction only proceeds to the ground state. Other commonly used reaction nuclei are ^{10}B and ^{3}He. The cross-sections involving these target nuclei are presented in figure2.6. If now all the reaction products are stopped and detected, the response function would look like the sketch in figure 2.7 which shows a single full-energy peak at the Q-value.

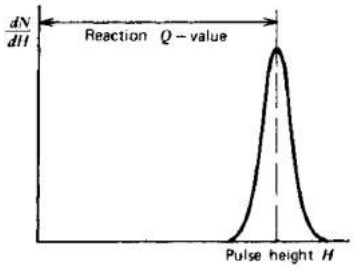

Figure 2.7: Sketch of response function with a detector with dimensions large enough to detect the reaction products after a slow neutron-induced nuclear reaction.[27]

2.2.2 Fast neutron detection

In contrast to the slow neutrons, spectroscopy can be done for fast neutrons with an energy greater than 1 eV. The detection principle is the same as for slow neutron de-

tection: a nuclear reaction takes place and the reaction products are directly detected. The kinetic energy of the reaction products will now be determined by the Q-value of the reaction and the initial kinetic energy of the incoming neutron. The reaction with ^{6}Lithat was discussed for slow neutrons applies also to fast neutrons in principle. Note that the probability for a fast neutron to interact with a ^{6}Linucleus decreases with increasing energy, as shown in the cross-section plot of figure 2.6. In the region of 250 keV, the cross-section reaches a resonance peak. The relatively high Q-value of ^{6}Lireaction with neutrons (4.78 MeV) comes is an advantage for the detection of thermal neutrons but puts a limit on the detection of fast neutrons. Only fast neutrons with energies above several hundred keV can be measured.

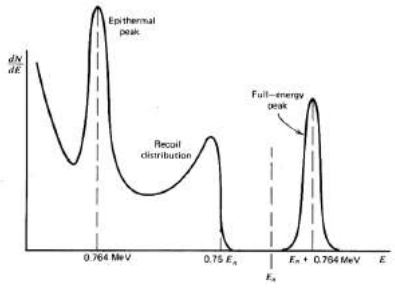

Figure 2.8: Sketch of response function with a detector with dimensions large enough to detect the reaction products after fast neutrons interacted with ^{3}He.[27]

The additional most common process for fast neutrons is elastic scattering. In a reaction, a part of the neutron's energy is transferred to the scattering nucleus. This results in a "recoil nucleus". For low energies, this recoil nucleus has too small energies to be detected. But once neutron energies reach higher than order keV, the recoil nuclei can be detected. As an illustration, the response function of fast neutrons interacting with ^{3}He target nuclei is shown in figure 2.8 where the Q-value of a neutron interaction is equal to 0.764 MeV. A similar figure could be drawn for the material under study: ^{6}Liwith Q-value 4.78 MeV. In figure 2.8, a peak appears at an energy equal to the Q-value plus the neutrons' initial kinetic energy, which originates from the nuclear reaction. In practice, it is common to see a second peak near the Q-value, which is induced by fast neutrons that lose energy along their way to become thermal neutrons that are more likely to interact with a ^{6}Linucleus. This peak is called the "epithermal peak". Besides these peaks, a pulse height continuum also appears in the spectrum of figure 2.8. This is the result of all the elastic scattering interaction of the neutron with the absorber material. In one elastic collision, neutrons transfer their energy only partially. The maximal energy a neutron can transfer in one interaction can be derived in a few steps [27]:

Conservation of momentum and energy for non-relativistic neutrons ($E_n \ll 939$ MeV) yields that the recoil energy of the nucleus is equal to

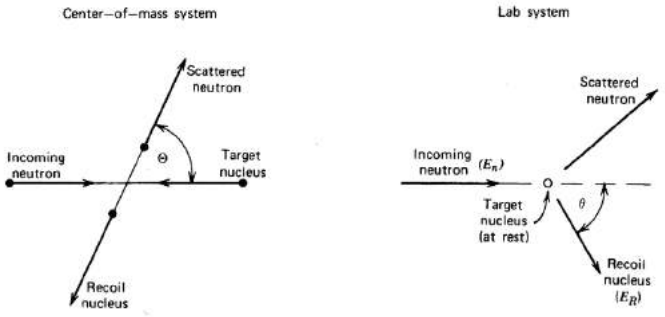

Figure 2.9: Diagrams for neutron elastic scattering in the laboratory frame and the center of mass frame.[27]

$$E_R = \frac{2A}{(1+A)^2}(1-\cos\Theta)E_n \tag{2.6}$$

with

A the mass of the target nucleus/ neutron mass,

E_n the kinetic energy of the incoming neutron in the laboratory frame,

E_r the kinetic energy of the recoil nucleus in the laboratory frame,

Θ the scattering angle of the neutron in the center of mass frame.

In order to convert this equation in the center of mass frame to the more familiar picture of the laboratory frame where the nucleus is at rest, the following transformation has to be used:

$$\cos\theta = \sqrt{\frac{1-\cos\Theta}{3}} \tag{2.7}$$

with θ the scattering angle of the recoil nucleus in the laboratory frame. The expression for the recoil energy then becomes

$$E_R = \frac{4A}{(1+A)^2}(\cos^2\theta)E_n \tag{2.8}$$

We can conclude that the transferred energy from the neutron to the nucleus is uniquely defined by the scattering angle. The recoil energy will be near zero when the neutron is only slightly deflected. This is the case where the scattering angle $\theta \cong 90°$. In case the collision happens head-on and the recoil nucleus travels further in the direction of the incoming neutron, the energy transfer is maximal and can be written by

$$E_{R,\max} = \frac{4A}{(1+A)^2}E_n \tag{2.9}$$

Target Nucleus	A	$\frac{E_R}{E_n}\|_{\max} = \frac{4A}{(1+A)^2}$
$^{1}_{1}$H	1	1
$^{2}_{1}$H	2	8/9=0.889
$^{3}_{2}$He	3	3/4=0.750
$^{4}_{2}$He	4	16/25=0.640
$^{6}_{3}$Li	6	24/49=0.490
$^{12}_{6}$C	12	48/169=0.284
$^{16}_{8}$O	16	64/289=0.221

Table 2.1: Maximum fractional Energy Transfer in Neutron Elastic Scattering [27]

The last column in table 2.1 expresses the maximal fraction energy the incoming neutron can transfer to the nucleus of interest. One can see that this fraction decreases with the mass of the target nucleus. The trend table 2.1 shows why it is interesting for neutron detectors to use light nuclei - and by preference hydrogen - as moderator materials.

Furthermore is it also of interest to look at the distribution of the neutron energy transfer between the two extreme cases. Above was already mentioned that a continuum of energies can be expected since all scattering angles are allowed. The shape of this energy continuum depends however on the probability that a neutron will be scattered in a certain direction. If $P(E_R)dE_R$ describes the probability of a recoil nucleus to get an energy between E_R and $E_R + dE_R$, then can be proven that $P(E_R)$ is given by

$$P(E_R) = \frac{(1+A)^2}{A} \frac{\sigma(\Theta)}{\sigma_s} \frac{\pi}{E_n} \tag{2.10}$$

with $\sigma(\Theta)$ the differential cross-section in the center of mass frame. An example is shown for ^{4}He in figure 2.10.
The shape that can be expected for the recoil energy continuum is the same as the differential angular cross-section for the neutron in the center of mass frame. For most target nuclei, $\sigma(\Theta)$ tends to peak slightly in the forward and backward directions.

2.2.3 Photon interaction mechanisms

This thesis will not separately address studies involving photons. However, because scintillators generate a significant amount of light, it is worthwhile to explore the three most important interaction mechanisms of photons in more detail.

Photo-electric absorption
During photoelectric absorption, an incident photon gets completely absorbed by an

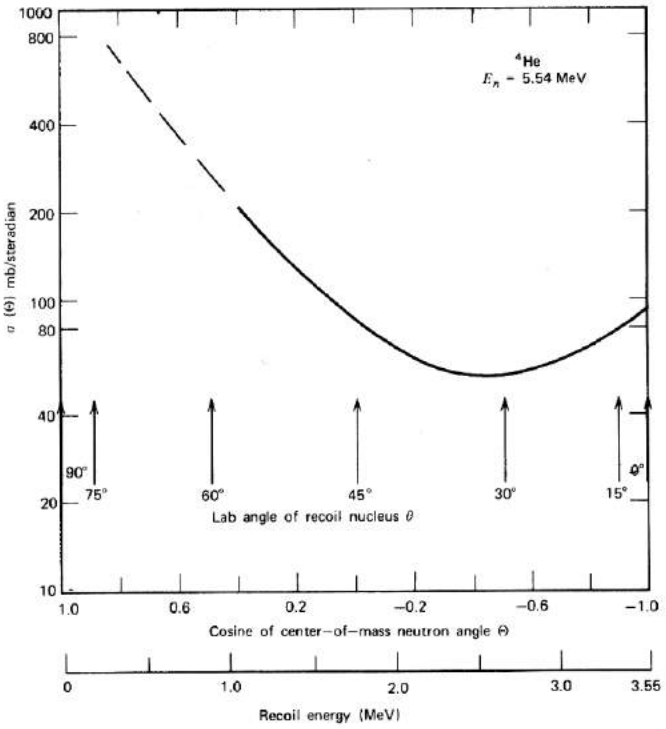

Figure 2.10: The differential cross-section for ^{3}He at a neutron energy of 5.54 MeV. Also indicated are the corresponding angle and energy of the helium recoil nucleus in the laboratory frame.[27]

atom. The atom then ejects a so-called photo-electron that has an energy equal to the incident photon energy minus the binding energy of this electron ($E_{e^-} = h\nu - E_b$). The interaction results besides the creation of a photo-electron also in an ionized atom with a vacancy. The vacancy will be filled as quickly as possible by capturing an electron from the medium and/or rearranging electrons from other energy levels of the atom. This reaction will therefore also be accompanied by the emission of one or more characteristic X-rays.

Compton scattering

Compton scattering occurs when a photon undergoes an inelastic collision with an electron. During the collision, the photon will transfer some of its energy to the electron. This electron is also known as the *recoil electron*. The incidental photon will be scattered at an angle θ relative to the original direction in which the photon was traveling. The transferred energy that the photon will pass through will be determined by this angle θ and is represented as

$$h\nu' = \frac{h\nu}{1 + \frac{h\nu}{m_e c^2}(1 - \cos\theta)} \tag{2.11}$$

with $m_e c^2$ the rest mass of the electron (0.511 MeV). If scattering takes place at a small angle, little energy will be transferred. The law of conservation of energy and momentum predicts that the maximum transferable energy occurs in case $\theta = \pi$. Since the Compton scattering interaction of a photon and an electron of an absorber atom depends on the number of electrons in the atom, we see the probability for this interaction to arise is linearly proportional to the atomic number Z.

Pair production

When the energy of the photon is greater than twice the rest mass of an electron (1.02 MeV), then it will become energetically possible to perform pair production. This interaction mechanism occurs in the Coulomb field of an atomic nucleus, causing the photon to disappear and be replaced by an electron-positron pair. The remaining energy that does not go into the creation of this pair ($E = h\nu - 1.02$ MeV) will serve as kinetic energy shared among the electron-positron pair. The positron will soon annihilate resulting in the emission of two annihilation photons. A straightforward expression for the probability of the pair production interaction mechanism is challenging to formulate, but it is roughly proportional to the square of the absorber's atomic number Z. As the energy of the photon increases, pair production will also become more important.

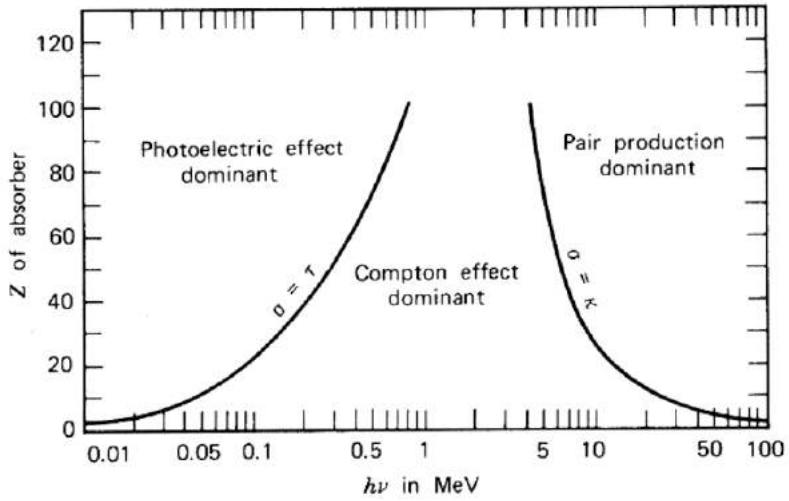

Figure 2.11: The importance of the three discussed photon interaction mechanisms as a function of the incident photon energy and the absorber's atomic number Z. [27]

Figure 2.11[25] shows which interaction mechanism dominates for a given photon energy and absorber material. The functions $\sigma = \tau$ and $\sigma = \kappa$ are not discussed further here. Still, it is interesting to look at the general behavior of these functions. At relatively low energies photoelectric absorption will predominate and at high energies pair production. The Compton effect dominates in the energy ranges in between.

2.3 Wavelength Shifting Fibers

To match the scintillation light spectrum to the SiPM spectrum, the scintillator cubes are connected to the SiPM via wavelength-shifting (WLS) fibers. Fluorescent organic molecules that are in the WLS absorb light originating from the scintillator and then isotropically emit secondary light of longer wavelengths. The decay time for such an excited molecule is typically of order nanoseconds. The good timing resolution from the scintillator is thus conserved.
The wavelength shifting fibers from the SoLi∂ experiment are of type BC-91A from St. Gobain. They consist of a core surrounded by a single cladding. These fibers are 3 mm $\times$3 mm in cross-section and are placed inside grooves of 5 mm $\times$5 mm that are aligned perpendicular along two faces of each cube[48].
To collect and transmit light from the scintillator to the Silicon photomultiplier as efficiently as possible, the refractive index of the WLS material must be carefully selected. The light in the WLS will often reflect. If a light ray incidents at an angle greater than the critical angle θ_c, total internal reflection will occur. However, if the incident angle is less than θ_c, the Fresnel reflection law predicts that the light will undergo partial reflection and partial transmission. The same statement stands for the scintillator. The situation is sketched in figure 2.12. The critical angle is determined by the refraction

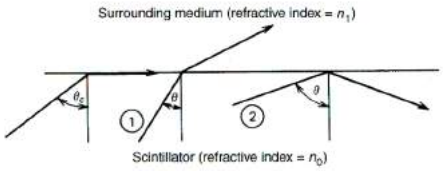

Figure 2.12: Reflection and transmission of light at scintillator surface.[27]

index of the medium of the WLS or scintillator (n_0) and its surroundings (n_1).

$$\theta_c = \sin^{-1}(n_1/n_0) \tag{2.12}$$

To minimize light escape from the edges of the WLS and optimize signal transfer, it is preferable to use a material with a refractive index significantly higher than that of air. Usually one chooses a material with a refractive index of around 1.5 (such as the refractive index of glass). To transmit the signal as completely as possible, an attempt will be made to match the refractive index at the contact points of the WLS with other

components. Scintillators therefore also usually have a refractive index of around 1.5.

2.4 Silicon Photomultiplier

After the photons from the scintillator are transported through the WLS, they are passed to the Silicon photomultiplier. The Silicon photomultiplier is a solid-state detector that converts electromagnetic radiation into an electric signal. It realizes a high gain and works with a relatively low bias voltage. The SiPM is sensitive to even single photons from the near-ultraviolet to the near-infrared range of the electromagnetic radiation spectrum. But before we go over to the structure and operation of the SiPM, the Geiger mode and SPAD are first briefly discussed [32].

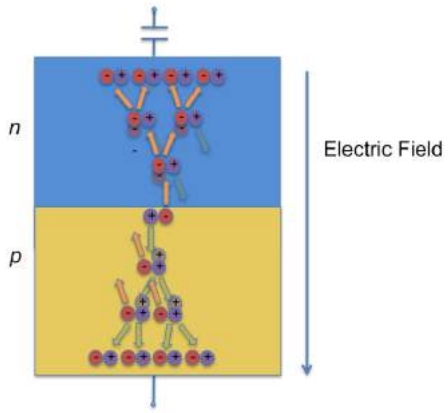

Figure 2.13: Diode operating in the Geiger mode.[32]

Let's consider a simple diode. The diode is made of silicon and is constructed to have a p-n junction. When a photon with a sufficient amount of energy hits the diode, it gets absorbed in the silicon and creates an electron-hole pair. If this happens in the depletion region, the electron will drift toward the cathode and the hole toward the anode. The movement of the charge carriers results in a current. If the voltage over the diode is set beyond the breakdown voltage, then the diode is said to be operating in the Geiger mode. This can be seen in figure 2.14. The p-n junction is now an avalanche region. This means that any charge carriers that are created in this region, are accelerated to such an extent that they will create other electron-holes through impact ionization along their way. The secondary created electron-hole pairs undergo the same faith and in this way, an avalanche is spreading throughout the silicon. The diode now becomes conductive. A macroscopic current can be detected by the induction of a single electron-hole pair.

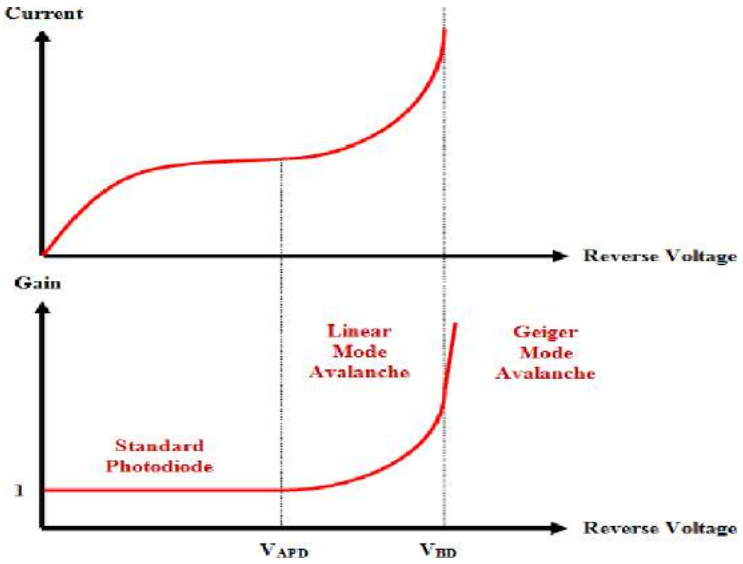

Figure 2.14: Different operation modes of a diode in a reverse bias vs. current plot.[33]

The diode is now referred to as a Single Photon Avalance Diode or SPAD. The current that is induced by a single photon in a SPAD will continue until it is stopped or quenched. If this was not the case, then the SPAD would not be able to detect sequential photons. A quenching resistor RQ in series with the SPAD is used to achieve the quenching. This resistor limits the current through the diode during breakdown. So as a photon falls onto the diode, causes a breakdown and it introduces a current that causes a voltage drop over the quenching resistor. On its turn, this resistor reduces the voltage over the diode to a value below the breakdown to stop the avalanche. The diode is reset to the beginning situation after it recharges back to the initial voltage and the next photon can be detected. The output pulses of the operation mode all have the same pulse height, even if multiple photons fall onto the diode at the same time. This operational mode of the diode does not provide any information on the magnitude of the incoming photons.

This lack of proportionality information can be overcome by the silicon photomultiplier by using a structure of independent units consisting of SPADs and quench resistors. Such a single unit is called a “microcell”. An overall scheme can be found in figure 2.15. When one microcell is struck by a photon, an avalanche is induced, and the same cycle as before is run over. The result obtained at the anode and cathode is the same as for a single SPAD with a quench resistor since every microcell operates independently from each other. But if now two microcells are hit simultaneously, the output at the cathode and anode will be the sum of the two microcells combined. The pulse height is twice the size of a single photon signal. The SiPM thus gives information on the amount of photons that fall onto the sensor as this is proportional to the

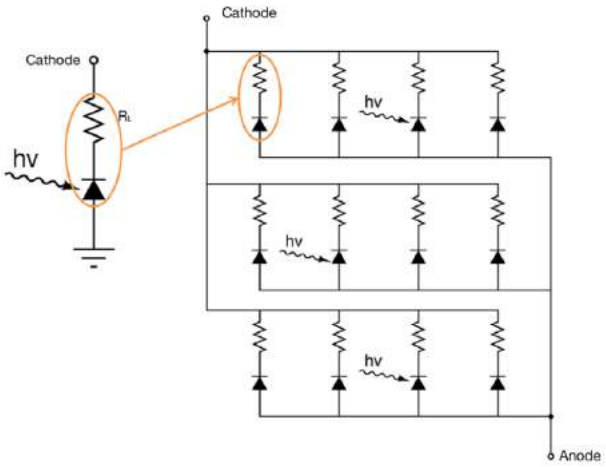

Figure 2.15: Schematic overview of microcells in a SiPM.[32]

number of triggered microcells.

Chapter 3

Approach by simulations

3.1 Geant4

Now the working principles of the detector components are better understood, their possibilities in applications can be explored. A compelling strategy involves implementing the contents into the program Geant4 and uncurtaining their capacities through simulations.

Geant4 is an open-source toolkit to simulate particles' passage through matter [34]. A worldwide collaboration of physicists and software engineers developed this toolkit to use in applications in particle physics, nuclear physics, medical physics, space engineering and accelerator design. It is written in C++ and offers a wide range of functionality including physics models, tracking, geometry and many more. It is interesting to go over a few aspects that were used in the simulation in this thesis.

The desired detector setup can be implemented using Geant4's material and geometry definitions. The scintillator material, polyvinyl toluene, of the cube, is already known by Geant4 under the name `G4_PLASTIC_SC_VINYLTOLUENE`. The default density for this material is 1.032 g/cm^3. The remaining properties of the scintillator such as the scintillation yield, absorption length for certain energies, etc can be implemented by hand. The ^{6}Li enriched neutron screen can be implemented by defining the isotopes that must be used and describing the abundance of this element in this detector component. Each element can be found in the Geant4 material database. In the following simulation results the neutron screen that was implementer consisted of 44.7% fluorine, 25.3% zinc, 21.9% sulfur and 8.1% ^{6}Li isotope. Finally, the cubes and screens can be wrapped with Tyvek by making use of the function `G4OpticalSurface`.
Figure 3.1a is a visualization of the detector components after applying the right dimensions to the components and placing them in the correct order. Figure 3.1b shows a single scintillator cube activated by a passing muon. When a visualization of a Geant4 simulation is represented in the following chapters, the scintillation light will not be shown so that the primary and secondary particles get accentuated.

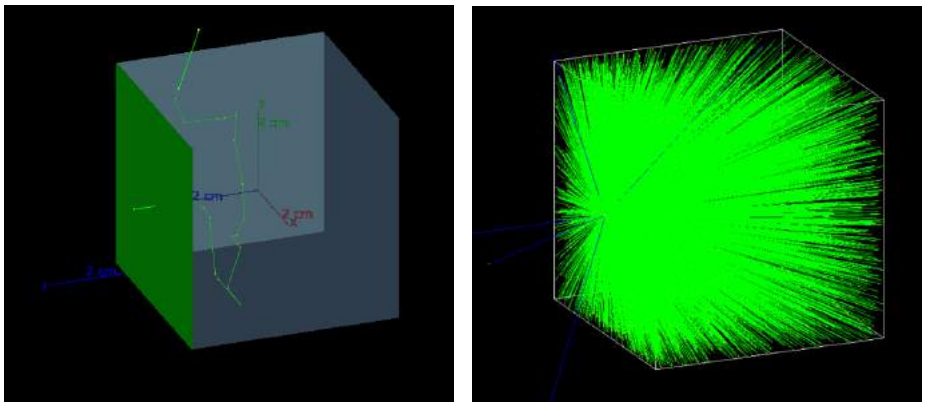

(a) Neutron (yellow) passing through the neutron screen (green) and entering the scintillator (grey).

(b) 1 MeV muon (blue) shot from left to right, causing scintillation light (green) inside the cube.

Figure 3.1: Visualization of the detector setups in Geant4.

Defining a physics list is one of the mandatory objects to perform simulations with Geant4. It specifies all the particles that will be used in the simulation together with a list of physical processes assigned to them [38]. It is an easy and flexible way to set up the physics environment.
The simulations in this thesis utilize two distinct physics lists, chosen based on the specific scenario. `FTFP_BERT_EMZ` is used in case charged particles such as electrons, muons and protons are passing through the detector setup. While `QGSP_BERT_HP` is applied in case neutrons are involved too.
Both physics lists can be broken down into pieces that each represent an approximation or model:

- `FTFP` stands for a combination of the Fritiof string model (applied for energies above 4 GeV) and the `G4Precompound` model that is used for de-excitation. The Fritiof strong model will not be discussed further as this would drift us away from the scope of this thesis. The additional `G4Precompound` model is used to simulate the de-excitation of nuclei. It can also be used for nucleon-nucleus interactions at low energies. [35][38]

- `BERT` is short for the Bertini Cascade model that is used for energies below 5 GeV. The Bertini model is based on the concept of the intranuclear cascade of hadrons and nucleons that are produced after a series of interactions within a nucleus. In essence, the model solves the Boltzmann equation for particles that are transported through a "gas" of nucleons and can therefore be seen as a classical model. The picture of a gas of nucleons is only true if the effective nucleon size is small and if we are dealing with only few collisions. When an incident

particle undergoes an elastic or inelastic interaction with individual protons or neutrons in a nucleus, the Bertini model generates a cascade of secondary particles. These secondaries can interact again with protons and neutrons, which produces further secondaries. This goes on until the secondaries escape the nucleus or are stopped and absorbed. The nucleus then de-excites by using evaporation and pre-equilibrium models.[36][38]

- `EMZ` is the `G4EmStandardPhysics_option4`. As the name suggests, it includes the standard low-energy electromagnetic physics. It can handle photons, electrons, positrons, hadrons and ions up to energies of 100 TeV and muons up to 1 PeV. It takes into account several photon processes: γ conversion into $e+e-$ pair, Compton scattering, photoelectric effect and Rayleigh scattering. Furthermore, it performs electron-positron processes like ionization, Coulomb scattering, Bremsstrahlung and positron annihilation. The additional part "option4" in the name represents the use of a combination of the most accurate EM models. Option 4 is the most precise option for the `G4EmStandardPhysics` of them all. Option 1 for instance is less precise but faster in performing the simulation.[37][38]

- `QGSP` is the Quark Gluon String model (>12 GeV) in combination with the `G4Precompound` model that is used for de-excitation. The Quark Gluon String model is an alternative to the Fritiof string model but they share the same datasets for cross-sections and the electromagnetic processes are also implemented in the same way.[38]

- `HP` is the High Precision neutron model (< 20 MeV) that is actually a low-energy neutron transportation model. It uses data-driven models to describe elastic scattering, inelastic scattering, neutron capture and fission reactions.[38]

Geant4 also allows to follow a particle along its trajectory during an event. At every step, certain properties of the particle can be requested. The outcomes considered in *Validating the simulation* all make use of this so-called `G4SteppingManager` function. It allows to follow a particle step by step.
The geometrical limits of a step are determined by the transportation processes and physical processes a particle undergoes. By pulling all processes together, the length of a step is calculated as the length at which an interaction is expected[39]. The function also determines whether the particle will stay in the same volume or will cross a boundary to a different volume before a potential interaction occurs. In figure 3.1a, the passage of a muon through the cube is visualized by a yellow trajectory. Every dot represents a stepping point.
At a considered step, the coordinates and the time at which the particle is located can be displayed. The step function is designed in such a way that when examining a particular step, one can always return to a previous step or the next step. In this way, it is possible to know what the kinetic energy of the particle is as well as the energy that

was deposited during the journey through matter. Moreover, one can also check which particle exactly is involved in that step. It could simply be that a particle has decayed and is no longer the same particle as initially induced. Furthermore, the function can also indicate which process has taken place between the current step and the previous step.

All these built-in functions and tools make Geant4 a very attractive strategy to investigate the behavior of the detector components and perform simulations.

Chapter 4

Validating the single cube simulation

Before jumping into complicated detector setup simulations, it is strategic to double-check the simulation acquired for a single cube. The simulated results will in this chapter be critically examined and these will then be compared to the physics. After this validation, the strengths and weaknesses of the components can be examined and then later built upon for more complex setups.

4.1 Energy deposition inside the scintillator

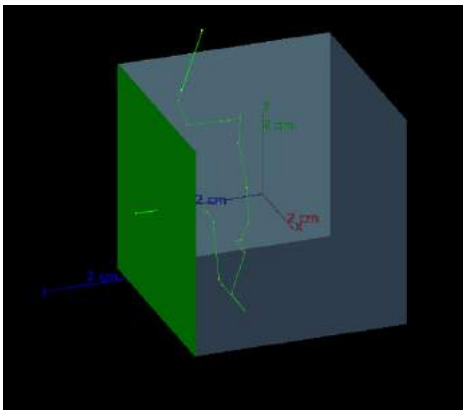

Figure 4.1: Visulaization of Geant4 simulation of a single scintillator with neutron screen.

After carefully implementing the SoLi∂ parts in Geant4, some results were obtained in order to get a better understanding of their operation. For starters, it is interesting to look at the behavior of particles through the scintillator material, more specifically to study the energy deposition of various types of particles as a function of their initial kinetic energy.

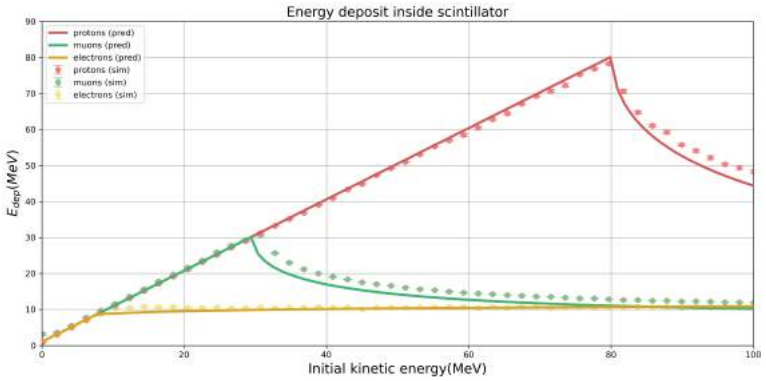

Figure 4.2: Energy deposition of particles with different initial kinetic energy in a single 5 cm $\times$ 5 cm $\times$ 5 cm scintillator.

The dots in figure 4.2 show the simulated energy deposition as a function of the initial kinetic energy of the incoming particles in a single 5 cm $\times$ 5 cm $\times$ 5 cm scintillator cube. The simulation is made by taking into account one cube and firing a specific kind of particle at it, namely electrons, muons and protons. On the horizontal axis of the plot, one can see the kinetic energy that was given to the particle. The mean energy deposition in the scintillator of a hundred particles with the same initial energy is then shown in this plot.
The behavior of this curve can best be described by the energy loss with the Bethe-Bloch formula [27].

The differential energy loss of a charged particle in a material divided by the differential pathlength is defined as the linear *stopping power S*:

$$S = -\frac{dE}{dx} \tag{4.1}$$

This formula can be rewritten with the classical expression that describes the specific energy loss, the "Bethe formula":

$$-\frac{dE}{dx} = \frac{4\pi e^4 z^2}{m_0 v^2} NB \tag{4.2}$$

where

$$B = Z\left[\ln\frac{2m_0v^2}{I} - \ln(1-v^2/c^2) - v^2/c^2\right] \tag{4.3}$$

with

v the velocity of the primary particle,

ze the charge of the primary particle,

N the number density of the absorber atoms,

Z the atomic number of the absorber atoms,

m_0 the electron rest mass,

e the electronic charge,

I the average excitation and ionization potential of the absorber.

The parameter I is experimentally defined for each element. The expression in equation 4.3 is energy-dependent and valid for different types of charged particles as long as their velocity remains large in comparison with the velocity of orbital electrons of the absorber atoms. Equation 4.3 does not include any correction terms.

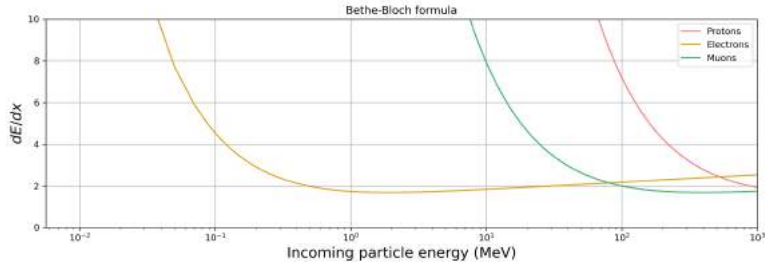

Figure 4.3: Visualization of the Bethe formula as described in equation 4.2.

The energy loss can then be determined by integrating the stopping power S over the thickness of the material and plugging in the incoming particles' velocity. This is done for the same energy range as the simulation that was discussed above. The result is plotted in figure 4.2 for electrons, muons and protons and always labeled by (sim). One can see that there is an excellent agreement between the simulated data and the prediction that was made by this simple equation.
Both the simulated data and the prediction curves show a typical peak that can be described by two effects: the particle range and the decrease in energy loss (dE/dx) with increasing energy. The particle range represents the distance over which a particle loses all its energy in an absorber material. Behind this distance, particles will not penetrate the material further. The range depends on the type of particle, the initial kinetic energy of the particle and the type of absorber material the particle goes through. A charged

particle's range is defined as [40]

$$R = \int_{E_0}^{0} \frac{dE}{dE/dx} \tag{4.4}$$

and after plugging in equation 4.2, we get

$$R = \int_{E_0}^{0} \frac{m_0 v^2}{4\pi e^4 z^2 NB} dE \tag{4.5}$$

After a some calculation, one gets that the particle range is proportional to

$$R \propto \frac{E_0^{3/2}}{\sqrt{m}} \tag{4.6}$$

or with $E_0 = mv^2/2$

$$R \propto mv^3 \tag{4.7}$$

These two proportionality equations show some interesting features. Equation 4.6 shows that for different particles with the same initial kinetic energy E_0, the heavier particle will lose its energy quicker than lighter particles. While equation 4.7 points out the situation where two different particles with the same velocity v, the lighter particles will slow down and stop sooner than the heavier particles [40].
However, the particle range has to be considered together with the behavior of energy loss in the material to come to the result we obtained in figure 4.2. For low energies, one sees that the energy loss is linearly proportional to the incident particles' energy. This is the region where the particle range is less than the detector thickness. At the peak value, the particle's energy range becomes equal to the detector thickness (5 cm). This happens for protons at 81.01 MeV, for muons at 30.40 MeV, and for electrons at 9.60 MeV. After that point, the behavior changes because the particles move too fast through the material to integrate with the absorber atoms. Only a fraction of the incident particle's energy is deposited in the absorber and the remaining energy is carried away by the moving particle. A decrease in energy deposit with increasing particle velocity can then be detected.

4.2 Energy distribution neutron

Another question one might wonder is what the distribution of energy deposit will look like with these SoLi∂ parts. In other words, what is the energy distribution one can expect?

In the section on *Slow neutron detection* and *Fast neutron detection*, the theoretical energy distributions where already discussed. After implementing the neutron screen in Geant4, the simulation output should be compared with the discussion of these sections. Figure 4.4, shows the energy distribution of a thousand thermal neutron events with an initial kinetic energy of 0.45 eV. The conclusion can be made that the result of

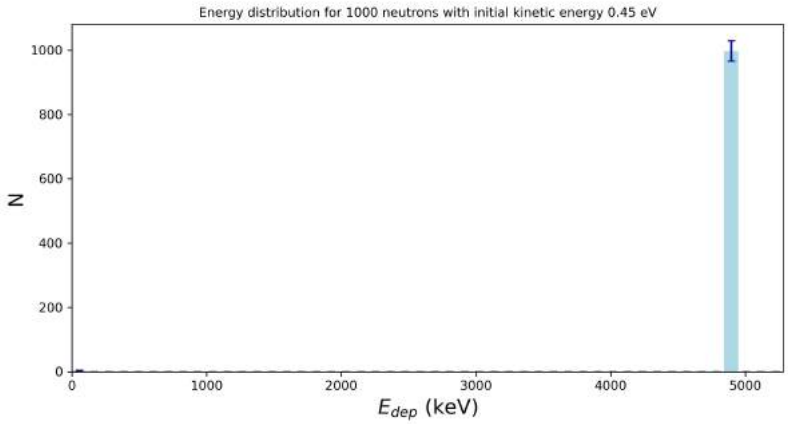

Figure 4.4: 1D distribution of the energy deposit for 1000 neutron event at an initial kinetic energy of 0.45 eV. The amount of particles is plotted against the energy deposition.

the simulation is in agreement with the prediction because the detector output for slow neutrons is expected to look like a single full-energy peak as sketched in figure 2.7. The cross-section of a neutron with such small energy and a ^{6}Li atom is relatively large and this indicates that numerous neutrons will interact with ^{6}Li. One can see that most of the events indeed included a reaction where an energy of 4.78 MeV is transferred to the reaction products: $^3_1$H and $^4_2\alpha$. Both reaction products are captured in the scintillator and have deposited all their energy. This results in the full-energy peak. Only very few neutrons did not interact with the screen and passed right through, hence the small bump at zero.

Fast neutron distributions are in comparison with slow neutron distributions not single peaked. To sketch this situation, a similar distribution plot is achieved by using neutrons with an initial kinetic energy of 250 keV. The cross-section for the reaction between neutrons and ^{6}Li is much lower now. Still, the full-energy peak, now located near the Q-value plus the initial kinetic energy (4.78 MeV + 250 keV = 5.03 MeV), is well distinguishable in the distribution plot in figure 4.5. A small epithermal peak near the Q-value appears as predicted to the left of the full-energy peak.
As expected, a lot of events will happen with lower energy deposition. Figure 4.6 zooms in on the lower energy events of this plot. This part of the distribution clearly shows the occurrence of the elastic scattering. The previously discussed formula 2.9 predicted that the maximum transferred energy to the recoil nucleus in a single elastic scattering event is equal to

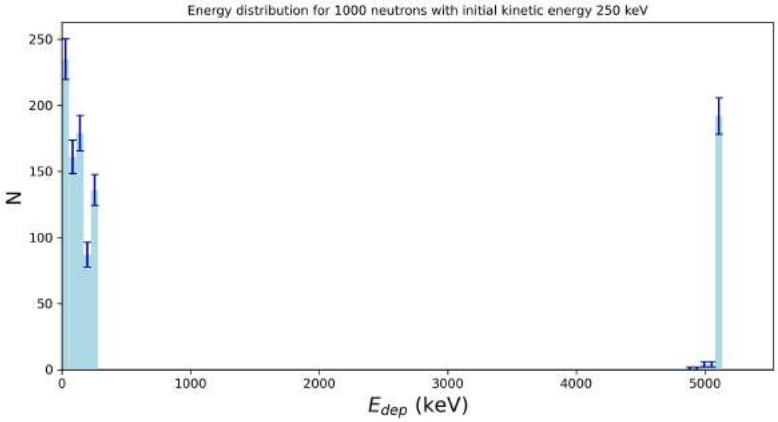

Figure 4.5: 1D distribution of the energy deposit for 1000 neutron event at an initial kinetic energy of 250 keV.

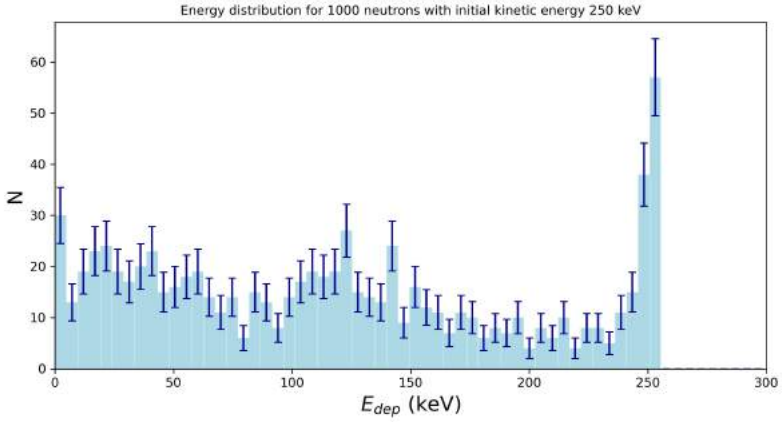

Figure 4.6: Zoom on 1D distribution of the energy deposit for 1000 neutron event at an initial kinetic energy of 250 keV.

$$E_{R,\max} = \frac{4A}{(1+A)^2} E_n = \frac{24}{49} \cdot 250 \text{ keV} = 122.5 \text{ keV}$$

Hence the somewhat higher bin at 122.5 keV. After this first collision, the particle interacts frequently inside the scintillator. The particle will therefore have the opportunity to release its full kinetic energy inside the cube. This is why we see the elastic scattering distribution edging at 250 keV.

4.3 Energy distribution charged particles

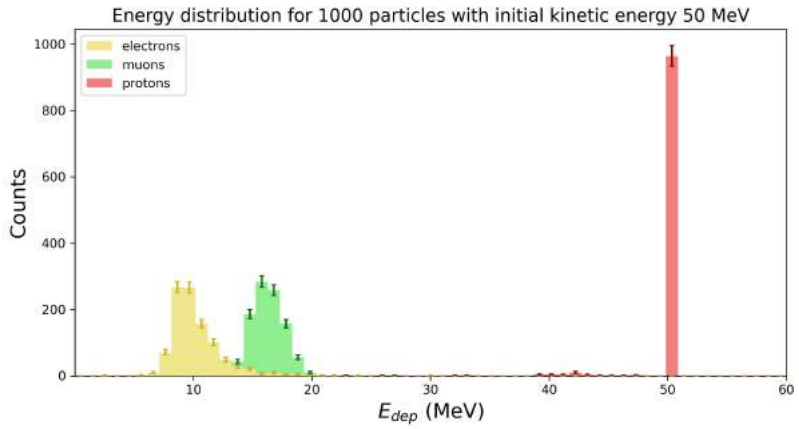

Figure 4.7: Energy distribution for protons, muons and electrons with initial kinetic energy of 50 MeV.

Figure 4.7 shows the simulated energy deposition of 1000 protons, muons and electrons with an initial kinetic energy of 50 MeV. The distributions all peak at other values and this is in agreement with the discussed behavior of the particles in figure 4.2. The proton distribution shows however some unexpected events around 43 MeV. The reason for this small bump lies in the occurence of a nuclear reaction between the proton and the organic scintillator. The ^{12}C(p,pα)^{8}Be reaction [41] has namely a Q-value of -7.366 MeV. Hence the reason why this bump appears around 50 MeV - 7.366 MeV = 42.634 MeV. Another possibility could be that as the proton passes through the material, it excites an atom and after de-excitation, a photon gets emitted. This photon can induce a similar reaction with the plastic scintillator material, namely ^{12}C$(\gamma, \alpha)^{8}$Be, which has the same Q-value of -7.366 MeV.
This barplot also shows that the energy deposit distribution of protons is narrow in comparison with those of muons and electrons. Together with figure 4.2, one can see that protons are still situated in the region where the particle range is less than the detector thickness. This means protons will efficiently lose all their kinetic energy in the material. Muons and electrons on the other hand are in a situation where they move rather fast to interact with the material and hence only a fraction of their energy is deposited. As this is dependent on how many events happened and what the transferred energy was, their energy deposition is not unambiguously defined, but according to a Landau distribution. This is in agreement with the expectations.

Unfortunately, it is unlikely to detect 50 MeV cosmic ray protons, muons and electrons at once since these energies come hand in hand with small fluxes. A more interesting plot to consider is the one shown in figure 4.8. For each particle type, it was determined

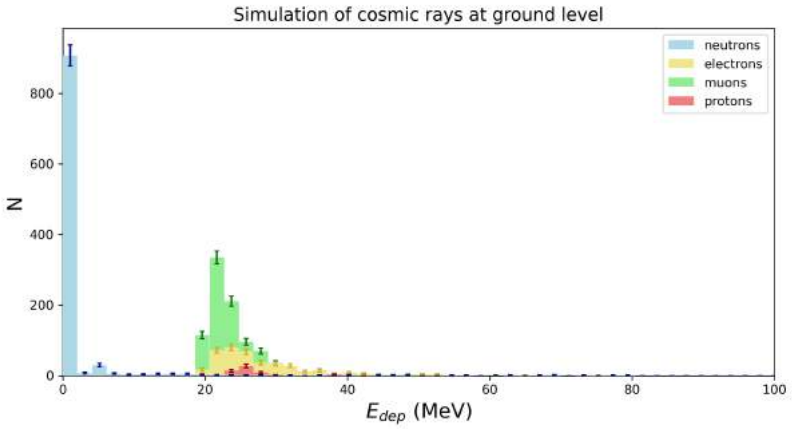

Figure 4.8: Energy distribution for neutrons, protons, muons and electrons with theoretically predicted rates in the cosmic ray spectrum.

what the energy range was in which the particle most commonly occurs in the cosmic ray spectrum and with what flux this appeared. These were then compared relatively to each other to arrive at a rough estimation of the expected cosmic ray spectrum at ground level that was used to obtain the energy distribution plot.

As expected, the most common signals are the ones from the low-energy neutrons. The high peak at the left represents their elastic scattering distribution. All the values lie under the keV region and are probably too small to produce a sufficient amount of photons in the scintillator. The datasheet of the EJ 200 material of the plastic scintillator describes that 1 MeV energy deposition in the scintillator corresponds to the production of 10 000 photons. If the rough estimation is made that 10 photons is the minimal required amount to produce a signal with the SiPM, a minimal threshold on the energy deposition will then be 1 keV. The elastic scattering distribution will in other words probably not be detected. Luckily, neutrons that interacted with the neutron screen come with a peak above 4.78 MeV and hence will manifest themself in the detected spectrum. Muons are the secondary most common particles but their peak overlaps with the ones from the electrons and protons. This indicates that it will be challenging to distinguish these particles using only a scintillator and a neutron screen.

In general can be concluded from this section that the energy deposition in the scintillator is quite precise in comparison with the particle's initial energies. Even though the elastic scattering distribution for neutrons will not always be detected, these particles will manifest themselves with the full-energy energy peak. For other particles, it would be quite challenging to make distinguishments between them.

Chapter 5

Other experimental setups

After seeing the operation of the scintillator and neutron screen in detail, we looked at the responses we can expect based on simulations. It soon became clear that these two components have high capacity as they can detect many particles in a wide energy range. Although electrons, muons and protons were discussed extensively here, other charged particles can also be detected with a scintillator. Think of charged kaons and pions that are also present in the Earth's atmosphere but which decay very quickly, with lifetimes respectively $\tau_K = 12.4$ ns and $\tau_\pi = 26$ ns.
The single cube with neutron screen setup was examined in the previous chapter. Keeping in mind the conclusions on the previous chapter, one can proceed with these advantages and disadvantages of the detector components to construct other experimental setups.

5.1 High-energy neutron detection

Since neutrons are neutrally charged particles, their detection requires to be performed indirectly. They have to interact with the ^{6}Li screen first to produce charged secondary particles. These can then be observed by the scintillator. But the cross-section for a neutron reaction to happen decreases with increasing neutron energy. This means that with access to a scintillator and a neutron screen, only thermal and low-energetic neutrons can be detected. Fortunately, alternative methods for fast neutron detection are available, namely the utilization of a moderator. A setup for this concept is shown in figure 5.1.

In general, a moderator can be used to slow down fast particles. Clearly, this is very useful to convert neutrons with high kinetic energy into thermal neutrons. Choosing an appropriate moderator material and thickness is crucial in this context. If the density of the moderator is not high enough, or if there are few elastic collisions between the neutrons and the moderator material, a neutron loses its kinetic energy less efficiently.

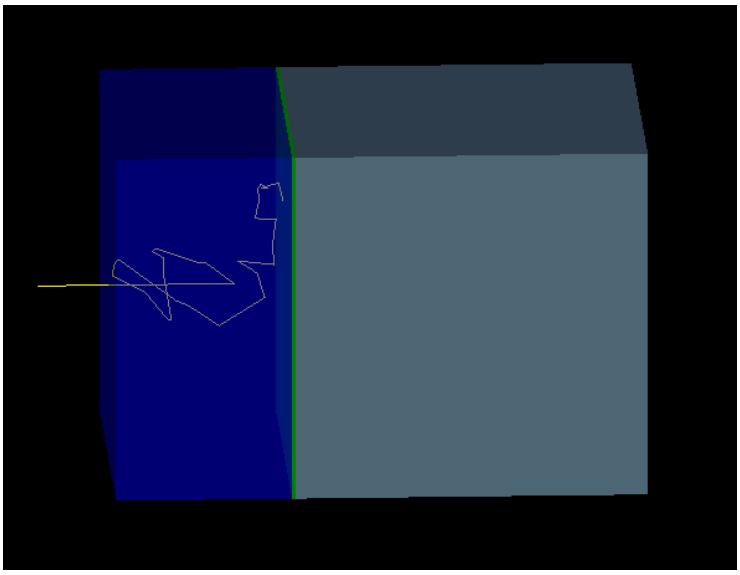

Figure 5.1: Visualization of Geant4 simulation of a neutron event with initial kinetic energy 10 keV in a 2.5 cm water moderator followed by a neutron screen and a plastic scintillator.

A large volume of this moderator is then required in order to still reach thermal neutrons. Because neutrons collide elastically many times in the moderator, their direction is constantly changing. If the moderator volume is too large compared to the volume of the scintillator, the chance of a neutron ending up in the detector volume will be low. On top of that, if neutrons are slowed down too much by the moderator, they can be absorbed and get lost in the end.

Figure 5.2 shows the results of simulations with different materials. Water, paraffin, concrete, lead, graphite and polyethylene were examined. The fraction of neutrons that are stopped as a function of the thickness of the moderator was studied. This was done for slow neutrons, epithermal neutrons and fast neutrons. Neutrons with random energy were taken, but for slow neutrons, the energy was always between 10^{-3} eV and 10^{-1} eV, for epithermal neutrons between 10^{-1} eV and 10^{4} eV and for fast neutrons between 10^{4} eV and 10^{7} eV.
The simulation results of figure 5.2 show us that water and paraffin are the most suitable materials to use as moderators. They allow neutrons to lose energy quickly and efficiently. In other materials such as polyethylene, it can be seen that the energy loss is a lot less efficient. In other words, a large volume of material will be needed to achieve the same effect as one would have with water or paraffin.

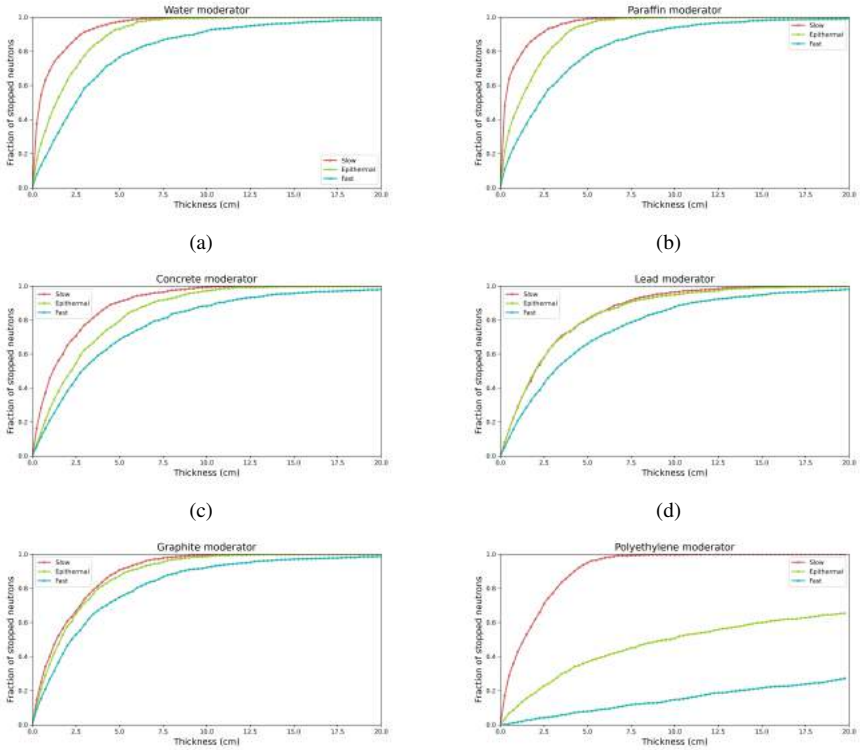

(a) (b)

(c) (d)

(e) (f)

Figure 5.2: Study of different types of moderator materials. The fraction of stopped neutrons is plotted as a function of the thickness of the material.

One can now further wonder how other particles would react to these efficient neutron moderators. As water and paraffin are the most effectual neutron moderators, it is interesting to further investigate these materials for the passage of electrons, muons and protons as well.

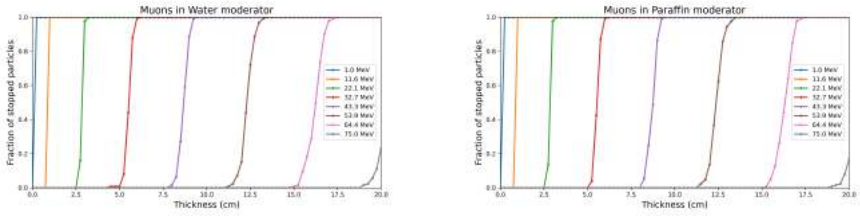

(a) Muons in water moderator (b) Muons in paraffin moderator

Figure 5.3: Geant4 simulation of muons in moderator

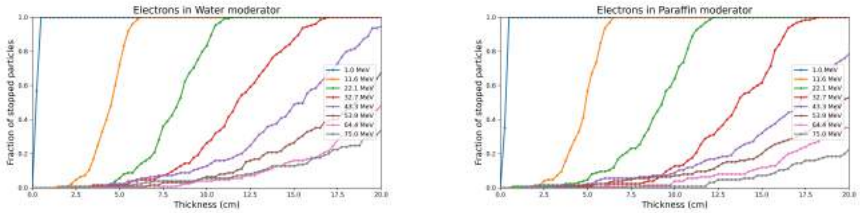

(a) Electrons in water moderator (b) Electrons in paraffin moderator

Figure 5.4: Geant4 simulation of electrons in moderator

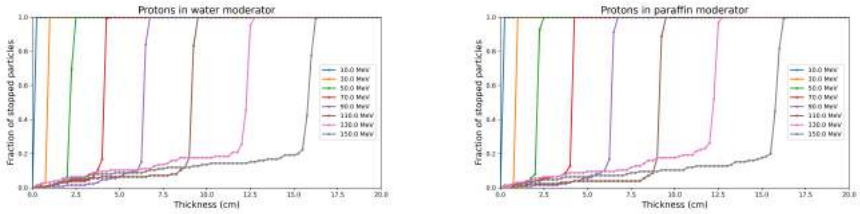

(a) Protons in water moderator (b) Protons in paraffin moderator

Figure 5.5: Geant4 simulation of protons in moderator

All the plots the figures 5.3, 5.4 and 5.5 show that particles of below a certain energy will be stopped in the moderator material. This means that a moderator of a specific thickness can put a lower limit on the observed energy of charged particles. Since the charged particles are slowed down by the moderator, the deposited energy is less directly related to the signal produced by the scintillator. Therefore, using simulations is rewarding for gaining better insight into the initial energy of the particles.

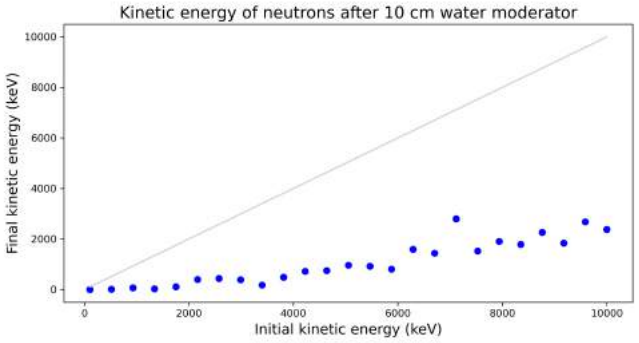

Figure 5.6: Fast neutrons getting slowed down by a 10 cm water moderator.

Purely as an example, the situation is sketched for a water moderator with a thickness of 10 cm. As can be seen in an earlier plot, slow and epithermal neutrons will not come through and the fast neutrons will be slowed down by this moderator. Figure 5.6 shows simulated data on how much the kinetic energy of the neutrons decreased. Each data point represents the mean value of 400 neutrons with the same initial kinetic energy. It can again be concluded that the water moderator successfully slows down the neutrons.

The plots in the figures 5.3a, 5.4a and 5.5a show that for a thickness of 10 cm, the minimum energy required to detect protons will be higher than that needed for muons and electrons. For muons, it is easy to put a lower limit on the initial energy. Namely, muons entering the moderator with a kinetic energy of at least 50 MeV will reach the scintillator. However, the plots for the protons and electrons are less straightforward and require some explanation first.

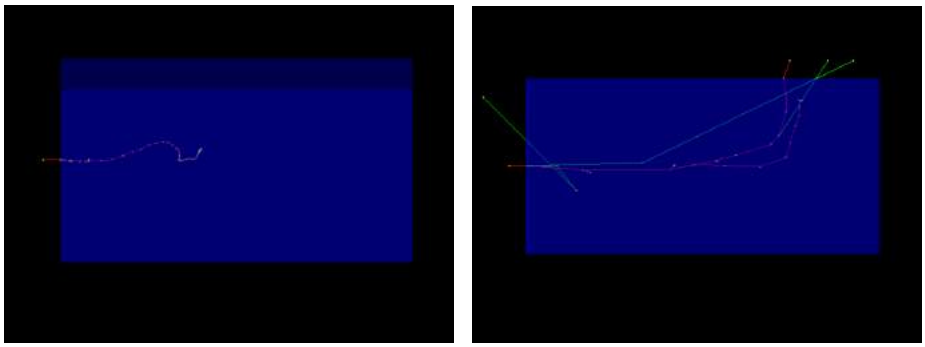

(a) Electron (red) with initial kinetic energy 5 MeV. (b) Electron (red) with initial kinetic energy 30 MeV.

Figure 5.7: Events inside a water moderator of 10 cm. The scintillator that should be placed on the right of the moderator has not been taken into account.

Figures 5.4a and 5.5a indicate that for increasing energy, only a fraction of the particles gets through the moderator. This makes it difficult to put a lower limit on the minimal particle energy that certainly will be observed. Approximating this problem by the usage of Geant4 simulations makes it able to dig deeper into what is happening in the moderator. Pictures of some randomly chosen events for an electron of 5 MeV and an electron of 30 MeV are given in figure 5.7. The plot in figure 5.4a predicted that the 5 MeV electron would completely be stopped by the moderator. This behavior is confirmed by figure 5.7a as the electron's track stops inside the moderator. For the 30 MeV electron, figure 5.4a explained that only a fraction of the electrons will reach the scintillator. Figure 5.7b illustrates this by showing that the electron possesses sufficient energy to undergo inelastic scattering with the water. Under these interactions, the lightweight electron can deflect and leave the moderator. If no other secondary created particles reach the scintillator as well, then there will not appear any signal. But if the electron does not get deflected too much, or if secondary particles reach the detector, then an observation can be made. With increasing initial energy, the fraction

of deflected particles decreases.

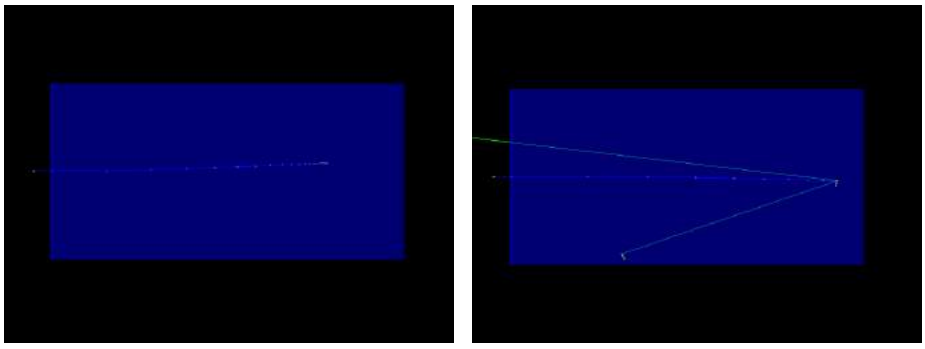

(a) Proton (blue) with initial kinetic energy 100 MeV. (b) Proton (blue) with initial kinetic energy 120 MeV.

Figure 5.8: Events inside a water moderator of 10 cm.

The plot in figure 5.5a shows that protons with a minimal initial energy of around 118 MeV can penetrate the moderator completely. However, just as for electrons, it seems like a fraction still does not reach the end of the moderator. To understand this behavior, the Geant4 simulation can be studied again. The situation for a 100 MeV and a 120 MeV proton can be seen in figure 5.8. It illustrates that protons do not interact as much as electrons and hence they do not easily get deflected. However, when a nuclear reaction takes place, the proton can get lost. For the event shown in figure 5.8b, this reaction was ^{16}O(p,pn)^{15}O. The effect seems to increase with increasing energy. If none of the secondary particles then reach the scintillator, the passage of a proton remains undetected.

In conclusion, the usage of a moderator helps to slow down neutrons so the chance of interaction with a ^{6}Li in the neutron screen becomes more probable. Adding a moderator to a detector setup influences the detection of other particles as well. If the initial kinetic energy is too low, the particle will be stopped in the moderator. Utilizing a moderator will thus put a lower limit on the initial kinetic energy that is required to detect a particle. However, simulations have shown that electrons can easily get deflected in certain energy ranges. Protons can undergo nuclear reactions in the moderator. Putting a lower limit on the initial kinetic energy can thus not always predict that a particle under these conditions will certainly be detected.

5.2 Sampling calorimeter

Calorimeters are detectors that fully absorb particles that pass through. The signal that comes out of this detector are measurement of the energy of the particle. As this particle passes through the calorimeter, it induces a shower. The shape and composition of the shower are dependent on the type and energy of the entering particle. Several detection mechanisms are used in calorimeters: scintillation, Cherenkov radiation, ionization, etc.[42]
Measurements with calorimeters depend on statistical processes. An average of N secondary particles are produced when a particle enters the detector. This N is proportional to the energy of the initial particle. When measuring the energy with a calorimeter, the resolution will be dominated by statistical fluctuations of N. One can see that increasing the energy of the incoming particle will improve the relative energy resolution:

$$\frac{\sigma_E}{E} \sim \frac{1}{\sqrt{E}} \tag{5.1}$$

This is in contrast with for instance tracking detectors that have a relative momentum resolution proportional to:

$$\frac{\sigma_p}{p} \sim p \tag{5.2}$$

These equations show that calorimetry is the preferable method to study high-energetic particles.

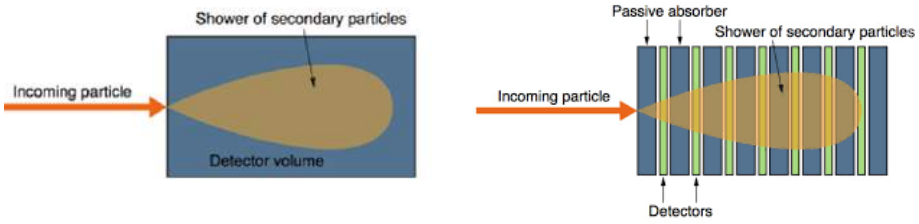

(a) Homogeneous calorimeter setup

(b) Sampling calorimeter setup

Figure 5.9: Types of calorimeters [42].

Generally, there exist two types of calorimeters: the homogeneous calorimeters and the sampling calorimeters. A sketch of the setups can be seen in figure 5.9a and 5.9b. Homogeneous calorimeters are made up of one material. This material has to be efficient as an absorbing material but also has to be able to pass a signal through the output. Scintillator materials such as BaF_2, CeF_3 and $PbWO_4$ are efficient but rather expensive. The $PbWO_4$ material is for instance used at the CMS calorimeters since it achieves the best possible energy resolution. A cheap alternative to a homogeneous calorimeter is the sampling calorimeter. These are constructed of alternating layers of absorber material and active detectors. The absorber material needs to have a high density to ensure

a high probability of interaction. Typically used absorbers are Fe, Pb and U. While plastic scintillators, silicon detectors, noble gas ionization chambers or gas detectors are typically used as active detectors. Since these detectors are easier to reconstruct with the available materials in this thesis, they will be discussed further. An implemented setup in Geant4 can be found in figure 5.10. One of the greatest advantages of the sampling calorimeter is that according to the application the absorber material and the detector material can be optimally chosen independent from each other. The more dense the absorber material is chosen, the more compact a setup can be. With this type of setup, one can observe how a particle showers and determine the energies at different locations within the shower by analyzing the signals from the scintillators placed between the absorber materials. A disadvantage of this type of detector is that only a fraction of the particle's energy is deposited in the detector layers and some part is lost in the absorber layers. The energy resolution for sampling calorimeters is also worse than for homogeneous calorimeters.

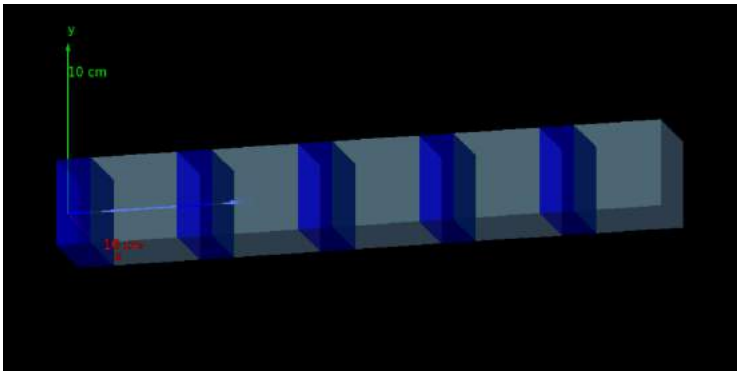

Figure 5.10: Visualization of Geant4 simulation setup for a sampling calorimeter. The absorber material is represented in blue, while the plastic scintillator are in grey.

To specify even further, a distinguishment can be made between electromagnetic calorimeters and hadronic calorimeters.

5.2.1 Electromagnetic showers

Electromagnetic calorimeters, or short EM calorimeters, measure the energy of electrons, positrons and photons [42],[43]. When high-energetic electrons or positrons enter the EM calorimeter, they interact via Bremsstrahlung and pair production. Photons interact via the photo-electric effect, Compton scattering and pair production. Via these processes, a cascade of secondary particles is created and the EM calorimeter aims to count the particles in the cascade. It does this by measuring the energy deposition, which is proportional to the number of particles in this cascade. All these above-mentioned processes that cause the development of the shower, occur with a dependence on the atomic number Z of the absorber. We will not go over the details but

in general, the following can be concluded [42]:

- Bremsstrahlung radiation and pair production dominates for particle energies above 1 GeV

- The shower develops further until the created secondary particles reach a critical energy E_c. This is defined as the energy at which:

$$\left(\frac{dE}{dx}\right)_{\text{rad}}(E_c) = \left(\frac{dE}{dx}\right)_{\text{ioniz}}(E_c) \tag{5.3}$$

  This point is circled in red in figure 5.11. The critical energy is strongly dependent on the material and scales as $1/Z$. As an example, E_c=7.1 MeV for Lead.

- As soon as secondary particles have energy below E_c, the energy loss becomes dominated by ionization, which can again be described by the Bethe-Bloch formula. The number of particles in the shower will then decrease because more and more particles get absorbed.

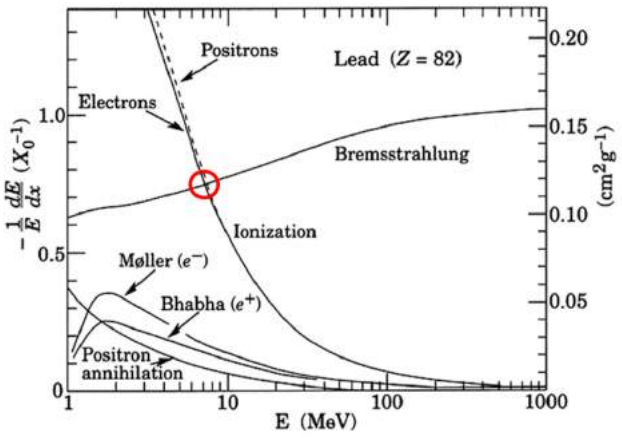

Figure 5.11: Fractional energy loss for electrons/positrons in Lead [44]

In general, one can say the development of the electromagnetic shower scales with the radiation length X_0. The radiation length X_0 of a material is defined as the mean length in centimeters over which the energy of an electron is reduced to $1/e \approx 37\%$ [43]. A useful approximation is

$$X_0 \approx \frac{180A}{Z^2} \tag{5.4}$$

This formula is dependent on the absorber material. For lead, $X_0 \approx 0.56$ cm. Since electrons lose their energy relatively fast when passing through a material, the EM calorimeters will not be constructed with large dimensions. Hence this is and ideal situation to construct with only a few scintillators and a few millimeters of material.

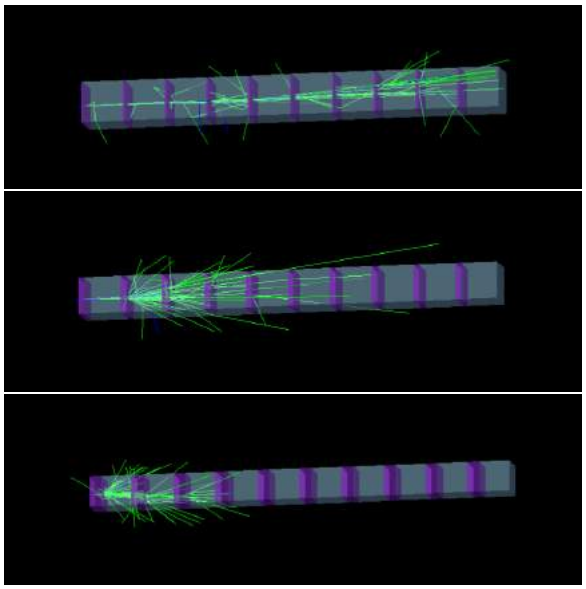

Figure 5.12: Visualization of Geant4 simulation electron event with an initial kinetic energy of 400 MeV in an electromagnetic sampling calorimeter. The absorber material is represented in purple, while the plastic scintillator are in grey. The thickness of the absorber in the picture from top to bottom are respectively 0.25 cm, 0.75 cm, and 2 cm.

Figure 5.12 shows in a few pictures of a Geant4 simulation how the electromagnetic shower induced by an electron varies with the thickness of the absorber. In this simulation, the electron's energy is set to 400 MeV. This energy was chosen randomly, but it is ensured to be adequately high to produce a shower. From top to bottom panel, the thickness of the absorber materials are set to be 0.25 cm, 0.75 cm and 2 cm. The top image therefore shows a shower event in which a layer of the absorber has a thickness smaller than the radiation length X_0. It is visible how stretched this shower will be. Due to the thinness of the absorber layers, the probability for the electron to interact is rather low. The showers will therefore contain fewer secondary particles than in the case of thicker absorber layers. On the other hand, it can be seen in the bottom image that a thicker material (2 cm) will absorb a large part of the shower. In this case, the shower will reach less deeply into the detector. The middle image shows a situation in between the two others. One can observe how the shower spreads gracefully in a cone shape across the detector.
The Geant4 simulations clearly help to determine what the detector setup should look like to achieve the desired result. Depending on which energy range one wants to mea-

sure and what the limitations on the detector dimensions will be, an ideal situation can be found by performing studies like this.

5.2.2 Hadronic showers

To measure the energy of charged and neutral hadrons, a hadronic calorimeter can be used. The same principles as for the EM calorimeter stand here still since hadrons passing through this detector still produce showers. These showers develop similarly to electromagnetic showers but since these are hadronic interactions, additionally strong interactions with the detector will also appear. The shower will therefore no longer scale with the radiation length X_0 but now with the nuclear absorption length λ_a. This λ_a is defined as the mean distance a hadron travels before undergoing an inelastic nuclear interaction [42]. It can be roughly estimated as

$$\lambda_a \propto 35 \text{ g/cm}^2 \cdot A^{1/3} \tag{5.5}$$

For Lead, this nuclear absorption length λ_a is around 17.1 cm. Since $\lambda_a \gg X_0$, hadronic calorimeters need to be a lot thicker than EM calorimeters. Hence only sampling detectors can be used to do hadronic calorimetry.

When a hadron enters a hadronic calorimeter, it undergoes a series of inelastic interactions with the material it passes through. These reactions create secondary particles that in their turn further undergo inelastic scattering and produce more particles. Under inelastic scattering, falls the production of mesons and baryons, spallation reactions, excitation reactions of the nuclei and nuclear reactions.
The most probable process of these is the spallation reaction. This violent reaction is the disintegration of the nucleus that results in the emission of protons, neutrons, α - particles and others. Commonly, the secondary particles have enough energy to interact further with other nuclei.
Under excitation reactions of the nuclei, we understand nuclear evaporation. In this process, nuclei in an excited state emit particles until the point where the remaining excitation energy is below the binding energy of the components in the nucleus. This typically happens in order of 10^{-18} seconds.
Elastic scattering events do not produce any secondary particles and will thus not promote the hadronic shower. As soon as particles do not have enough energy to interact with the absorber nuclei, they will further lose energy via ionization and excitation of absorber atoms. Because more interactions are involved, understanding hadronic showers is more complicated than electromagnetic showers.
This last statement can also be concluded after performing simulations with Geant4. Since the nuclear absorption length λ_a for lead was estimated at 17.1 cm, the first simulations looked at detector setups with large dimensions. Figure 5.13 shows lead layers of different thicknesses, followed by a layer of 3x3x1 stacked scintillator cubes. The initial kinetic energy for the protons was randomly chosen to be 2 GeV. In general, it

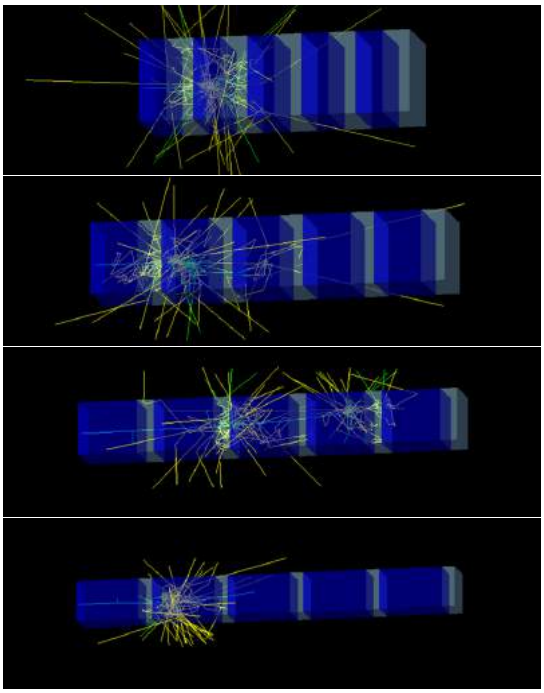

Figure 5.13: Visualization of Geant4 simulation proton event with an initial kinetic energy of 2 GeV in a hadronic sampling calorimeter. The absorber material is represented in blue, while the plastic scintillator are in grey. The thickness of the absorber in the picture from top to bottom are respectively 5 cm, 10 cm, 17 cm and 24 cm.

can be concluded that a hadron shower spreads widely compared to the narrow cone shapes formed by electromagnetic showers. Additionally, it seems that the place where a shower starts is not predictable. The reaction sometimes takes place at the beginning of the detector, and sometimes somewhat deeper. Occasionally very few secondary particles are created while in other events an explosion of secondary particles occurs.

Because yellow tracks in the simulation indicate neutrons, one can deduce from the figures that hadronic showers are accompanied by the release of many neutrons. This suggests indeed that a spallation reaction took place. With the currently presented Geant4 simulations for the hadronic sampling calorimeter, there will not be jumped to conclusions considering the wide fluctuations that are observed. To provide more clarity on this topic, further research is required. A similar deduction can be made for other particles. Events of a 2 GeV kaon and pion can be seen in figure 5.14, but the simulations generally come down to the same results as for protons: hadronic showers are less neath than electromagnetic showers.

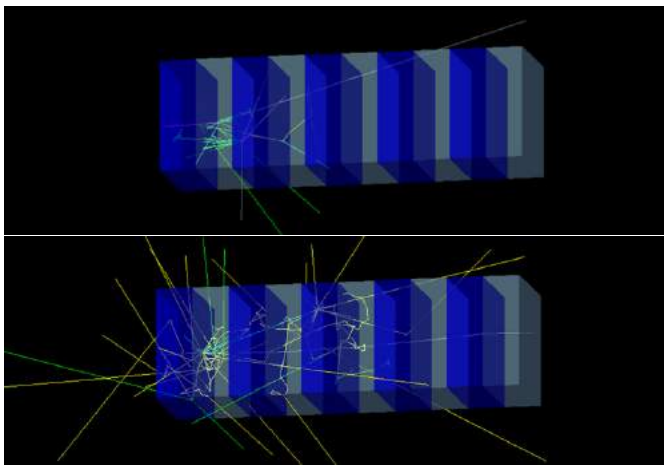

Figure 5.14: Visualization of Geant4 simulation pion (top panel) and kaon (bottom panel) event with an initial kinetic energy of 2 GeV in a hadronic sampling calorimeter. The absorber material is represented in blue, while the plastic scintillator is in grey. The thickness of the absorber in the picture are 5 cm.

5.3 Tracking detector

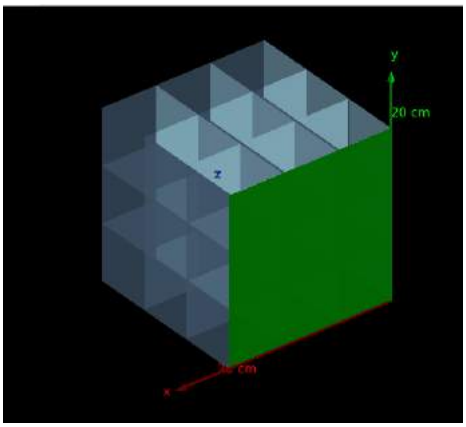

Figure 5.15: Setup with 3×3×3 scintillator cubes.The neutron screen is only applied to one side of this setup.

When investigating natural radiation, it is useful to know where the particle originates from. The flux of the particles in the cosmic ray depends on the angle at which measurements are performed. It might also be conceivable that a particle departed from the ground and reached the detector. To gain insides on this property, tracking is required. Tracking is the reconstruction of the path of a particle. Stacking several scintillator cubes in a three-dimensional geometry is the way to approach this. An example of a 3×3×3 scintillator cube setup can be seen in figure 5.15. In the next sections, the situation with and without wrapping every cube with tyvek are discussed.

5.3.1 Without tyvek wrapping

One can perform measurements with the 27 cubes stacked in a construction of 3×3×3 scintillators on top of each other, without using any tyvek. The tyvek is in generally used to isolate a cube so no scintillation light is lost or will activate surrounding cubes. Without the tyvek, one can expect that a lot of cubes will be activated and provide a signal. As an illustration, the situation is drawn for neutrons, muons, electrons and protons. Their initial kinetic energies are taken at energy values that commonly appear. For neutrons, a simulation was made at 250 kev, for muons at 2 GeV and for electrons and neutrons at 100 MeV. Figures 5.16, 5.17, 5.18 and 5.19 present in (a) the visualization of the Geant4 simulation, (b) the reconstruction that was made from the obtained data without a threshold and (c) with a threshold of 1 keV, which corresponds to a scintillation signal of 10 photons as a minimal value to observe a signal with the SiPM. The blue line in the reconstruction figures indicates the initial particle direction that was implemented in Geant4.

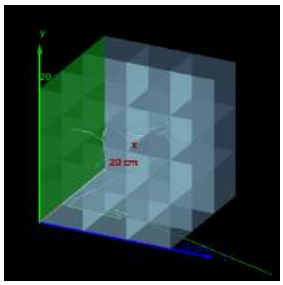

(a) Geant4 visualization

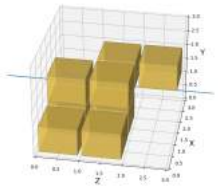

(b) Reconstruction (0 keV)

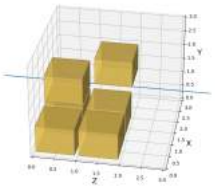

(c) Reconstruction (1 keV)

Figure 5.16: Tracking of a 250 keV neutron event without tyvek wrapped cubes

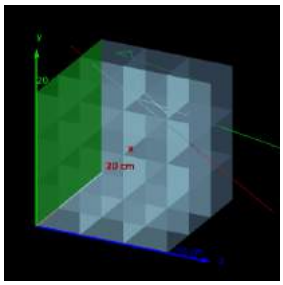

(a) Geant4 visualization

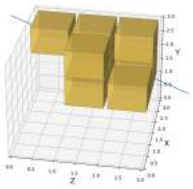

(b) Reconstruction (0 keV)

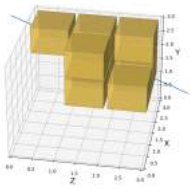

(c) Reconstruction (1 keV)

Figure 5.17: Tracking of a 2 GeV muon event without tyvek wrapped cubes

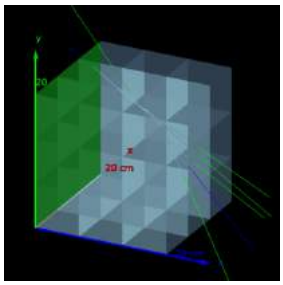

(a) Geant4 visualization

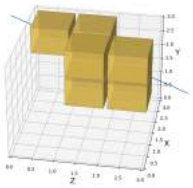

(b) Reconstruction (0 keV)

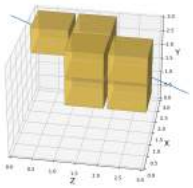

(c) Reconstruction (1 keV)

Figure 5.18: Tracking of a 100 MeV electron event without tyvek wrapped cubes

Figure 5.16 shows how a neutron reacts with the ^{6}Li in the neutron screen. This causes the creation of reaction products that can in their turn be detected with the scintillators. The reaction products seem to scatter around very often and hence many scintillator cubes will be activated. After applying the threshold, the number of activated cubes seems to be reduced. In this way, a general overview of the passing particle can be made. However, the track is somewhat smeared out but still, a conclusion can be made from what side of the setup the neutron originated from.

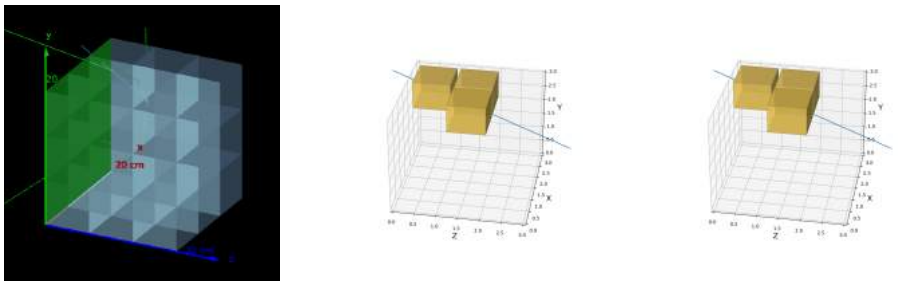

(a) Geant4 visualization (b) Reconstruction (0 keV) (c) Reconstruction (1 keV)

Figure 5.19: Tracking of a 100 MeV proton event without tyvek wrapped cubes

The muon track reconstruction however is more precise. From figure 5.17, it is clear that the 2 GeV muon passed through the whole setup. Along its way, it activated the cubes it passed through and some of the neighboring cubes. Applying the 1 keV threshold does not affect the conclusion.
A similar conclusion can be made for the electron track reconstruction. The electron passing through the scintillators goes along with the production of many photons. This can also be seen in figure 5.18 (a) as the green track represents photons and the blue tracks the electron.
The proton with the same initial kinetic energy as the electron penetrates less deeply in the detector setup. The track thus seems more simple.

5.3.2 With tyvek wrapping

When wrapping every cube in Tyvek, it is expected that fewer cubes will be activated when a particle comes through. Active volumes become more isolated from their neighbors. This behavior can be seen by making a comparison with the previous section. For the neutron event, figure 5.16 showed 8 activated cubes without a threshold and 6 activated cubes with a threshold at 1 keV. Figure 5.20 clearly shows the Tyvek wrap at work. Only 3 cubes are activated without any threshold and just 1 cube when the threshold is applied. The track reconstruction is very effective in this situation as the location of the neutron entering the cube can be traced.
The number of activated cubes for the muon event in figure 5.17 also reduced in comparison with figure 5.17. A similar statement can be made for the protons and electrons. A setup with Tyvek wrap is the most suitable way to approximate the tracking of particles through the scintillators.

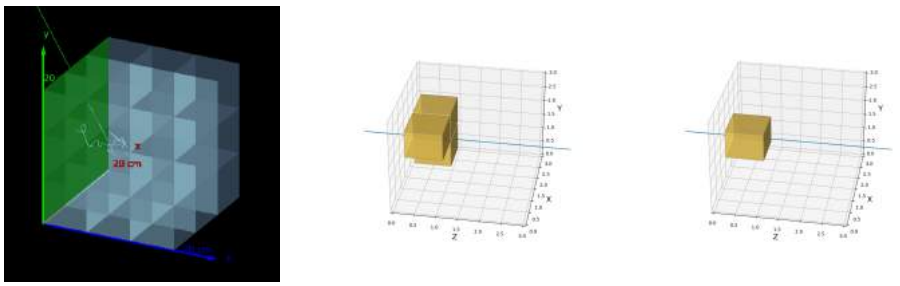

(a) Geant4 visualization (b) Reconstruction (0 keV) (c) Reconstruction (1 keV)

Figure 5.20: Tracking of a neutron event in setup with tyvek wrapped cubes

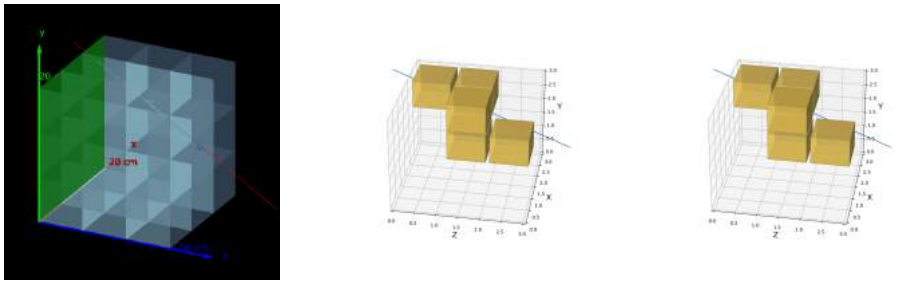

(a) Geant4 visualization (b) Reconstruction (0 keV) (c) Reconstruction (1 keV)

Figure 5.21: Tracking of a muon event with tyvek wrapped cubes

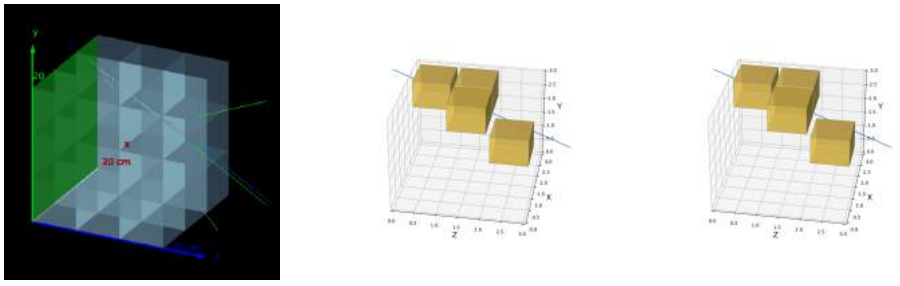

(a) Geant4 visualization (b) Reconstruction (0 keV) (c) Reconstruction (1 keV)

Figure 5.22: Tracking of a electron event with tyvek wrapped cubes

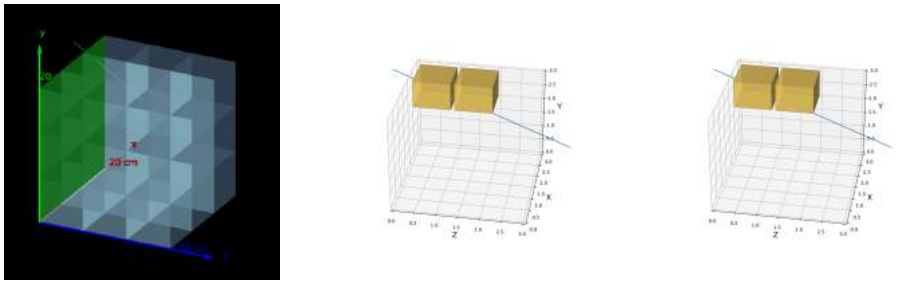

(a) Geant4 visualization (b) Reconstruction (0 keV) (c) Reconstruction (1 keV)

Figure 5.23: Tracking of a proton event with tyvek wrapped cubes

5.4 Planes of cubes: muon lifetime

One of the greatest advantages of organic scintillator detectors is their fast response to the passage of charged particles. It is therefore interesting to get started with this feature. Scintillators namely offer the possibility to determine the lifetime of muons.

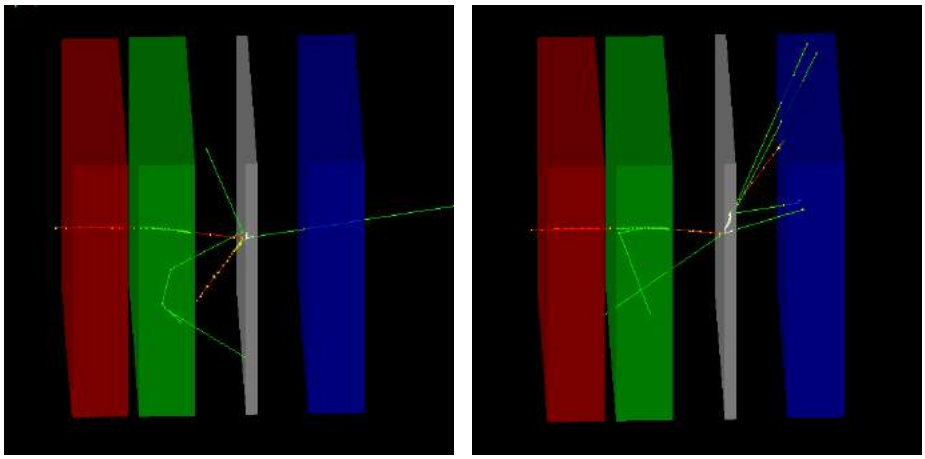

(a) e^- or e^+ emitted backward direction

(b) e^- or e^+ emitted forward direction

Figure 5.24: Geant4simulation of scintillator setup to determine muon lifetime. The red scintillators indicated plane (A), green scintillators plane (B) and blue scintillators plane (C).

To achieve this, a geometric arrangement of three large surfaces of scintillators and a metal plate is required. The first two scintillator planes will henceforth be called (A) and (B) and are placed parallel to each other. Their time response is used to indicate a start signal. As soon as a muon flies through both scintillators, a coincidence event is observed and a clock starts. The muon then flies further onto the metal plate. This metal plate is arranged parallel to the (B) plane. If a suitable material is chosen with a high density, the muon will be trapped therein and decay. In this example, an Aluminum plate with a thickness of 1 cm and density $\rho = 2.699$ g/cm^3 is utilized. The muon decay happens in the metal plate via a weak interaction and can be written in formula form as:

$$\mu^- \rightarrow e^- + \bar{\nu}_e + \nu_\mu \tag{5.6}$$

$$\mu^+ \rightarrow e^+ + \bar{\nu}_e + \nu_\mu \tag{5.7}$$

Since neutrinos are uncharged particles and they react only weakly with material, it will unfortunately not be plausible to detect them with the scintillators. However, it is possible to observe the electron or positron with the scintillators. To optimally detect

the electron or positron, a third scintillator plane is positioned parallel to and on the other side of the metal plate. We call this plane (C). The whole setup can be considered in figure 5.24. Because the electron or positron can be detected in both the backward and forward directions, the detection of plane (B) or plane (C) will transmit a signal to stop the clock. Botch cases are illustrated respectively in figure 5.24a and 5.24b.

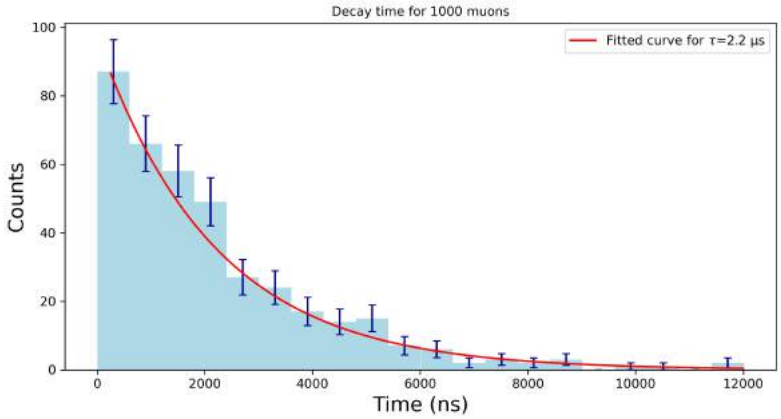

Figure 5.25: Geant4 simulation with setup to determine the muons lifetime. This is the time distribution plot of 1000 muon events (blue) together with the fitted exponential decay curve (red).

The blue bars in figure 5.25 illustrate the events of 1000 muons. The observed time was plotted as a one-dimensional distribution. Afterwards, a fit with function:

$$N = N(0)\exp(-t/\tau) \tag{5.8}$$

was performed. In this function, N refers to the number of observed muons at a certain time t, $N(0)$ is the number of mons at time $t = 0$ and τ is the lifetime of a muon. After fitting this function to the simulated data, a lifetime of approximately 2.2 μs was found for the muon. This is in perfect agreement with the theoretical value of $\tau_\mu = 2.1969811(22)$ μs[1].

Chapter 6

Conclusion

This thesis aimed to explore the possibilities of retired SoLi∂ components. The most obvious and accessible particle source to use with these components is natural environmental radiation. This consists of a whole zoo of particles that occur in various energy domains. The most prominent sources are the particles received from cosmic rays, more specifically the cosmic ray muons. However, since low-energy neutrons are dominant in natural environmental radiation, they certainly cannot be left out.
Since blindly taking data and then determining which particle with which energy was detected is impractical, a different approach was necessary. The Geant4 toolkit was invaluable in this regard. After carefully implementing each component in the program and selecting the appropriate physics lists, an investigation using simulations was established. This research began by inspecting a single scintillator cube to examine how this detector responds to the passage of charged particles. It soon became clear that the scintillator is capable of detecting all possible charged particles across a wide energy range. Subsequently, a neutron screen was added, and the same procedure was applied to understand its response. In addition to the already detectable particles, this screen made neutrons visible, particularly in the low-energy region. This is precisely the area that is most common in natural environmental radiation.

The next step to get closer to the natural environmental radiation was to detect different particles together. The limits of a single scintillator with a neutron screen emerged here. Since it became challenging to say more about which particles were detected, the single cube setup was left as it was. Consequently, the focus shifted towards other experimental setups that could provide even better insight into simulated data provided by the environmental radiation.

First, efforts were made to identify a method that would allow for the detection of fast neutrons since the cross-section for neutrons with ^{6}Li decreases with increasing neutron energy. The use of a moderator allows to slow down neutrons so a reaction with the neutron screen is more probable. The use of a moderator has however consequences for the detection of other particles. It namely sets a minimum value on the energy of particles that can be detected by the scintillator. This energy can be deter-

mined unambiguously for muons, but protons and electrons experience more reactions in this moderator than muons, so it must be taken into account that these particles do not always reach the detector through the moderator. For electrons, the reason lay in the constantly changing direction due to interaction with the moderator material. Electrons therefore have a significant chance of leaving the detector. While protons have the possibility to undergo nuclear reactions. If no secondary particles reach the detector volume, a proton signal is consequently lost.

Another way to map which particles pass through the detector is by constructing a sample calorimeter. This detector ensures that the particle in question will shower. For electrons and positrons, a careful choice of thickness in absorber material can ensure that only particles with a suitable energy shower in a desired manner. The use of Geant4 simulations before setting up a construction is highly recommended. The situation for hadrons was left inconclusive and further research is required.

The main purpose of the tracker setup was not to say anything more about the particle energies, but rather about the direction of origin. Natural environmental radiation comes to us from all angles and this was not taken into account so far. By stacking $3\times3\times3$ scintillator cubes on top of each other and then looking at which cubes are activated, a track reconstruction could be done. Research setups with and without Tyvek wrap made it clear that the most appropriate way to achieve accurate tracking was the setup with the use of Tyvek. The wrapping namely prevents leaking of the scintillation light into neighboring cubes.

Ultimately, a setup was developed to measure the lifetime of a muon. Given that scintillators are known for their fast operation and excellent timing resolution, this advantage can be effectively utilized. Simulations pointed out that this experimental setup can indeed simply determine the lifetime of a muon.

Note that in the discussed setups, photons were never explicitly taken into account. The experiments were performed in a completely dark environment. This is an important facet that is still missing from the obtained results.

The overall conclusion is that with scintillators and neutron screens, various setups can be created to explore different aspects of natural environmental radiation. Depending on which part of the spectrum one is interested in, a specific setup can be further investigated. Simulations such as those performed using Geant4 will be highly beneficial in optimizing these setups for more specific purposes. Note that before these components can be used in practice, they still need to be connected to the wavelength shifters (WLS) and the silicon photomultiplier (SiPM) to provide an electrical signal. The evolution of the signal through these components was not studied here. In these setups, no conclusions were drawn about the expected magnitude of the electrical signal. Further studies on optimizing these setups are recommended. Properties such as the conversion from photons to an electric signal, optimal thickness of the Tyvek wrap, signal noise, etc are left to be investigated further.

Bibliography

[1] Thomson, M. (2013). Modern Particle Physics. Cambridge University Press.

[2] The standard model. (2024, 29 april). CERN. https://home.cern/science/physics/standard-model#:~:text=The%20Standard%20Model%20includes%20the,all%20of%20the%20matter%20particles.

[3] Federal Agency for Nuclear Control. (2019). SURVEILLANCE OF THE TERRITORY & NATURAL RADIATION SERVICE [Report]. https://fanc.fgov.be/nl/system/files/2019-12-10-annual-report-2018-srt-en-final.pdf

[4] Cern. (2021, 27 september). A discovery of cosmic proportions – CERN Courier. CERN Courier. https://cerncourier.com/a/a-discovery-of-cosmic-proportions/

[5] Hillas, A. M. (2013). Cosmic Rays: The Commonwealth and International Library: Selected Readings in Physics. Elsevier.

[6] Karttunen, H., Kröger, P., Oja, H., Poutanen, M., & Donner, K. J. (2016). Fundamental Astronomy. Springer.

[7] Kachelriess, M. (2008). Lecture notes on high-energy cosmic rays. arXiv (Cornell University). https://doi.org/10.48550/arxiv.0801.4376

[8] figure 1-An illustration of the Shower of Particles Produced by Cosmic... (z.d.-b). ResearchGate. https://www.researchgate.net/figure/An-illustration-of-the-Shower-of-Particles-Produced-by-Cosmic-Ray-Collisions-From-Coan_fig1_317318317

[9] Ziegler, J. F. (1996). Terrestrial cosmic rays. IBM Journal Of Research And Development, 40(1), 19–39. https://doi.org/10.1147/rd.401.0019

[10] Grieder, P. (2001). Cosmic Rays at Earth. Gulf Professional Publishing.

[11] Murty, D. S. R. (1953). East-west asymmetry of cosmic rays. Proceedings Of The Indian Academy Of Sciences. Section A, Physical Sciences, 37(2), 317–320. https://doi.org/10.1007/bf03052714

[12] Hewitt, J. E., Hughes, L., Mccaslin, J. B., Stephens, L. D., Rindi, A., Smith, A. R., Thomas, R. H., Griffith, R. V., Welles, C. G., & Baum, J. W. (1976). Ames collaborative study of cosmic ray neutrons. STIN, 76, 16007. https://ntrs.nasa.gov/api/citations/19760008919/downloads/19760008919.pdf

[13] Abbrescia, M., Avanzini, C., Baldini, L., Ferroli, R. B., Batignani, G., Battaglieri, M., Boi, S., Bossini, E., Carnesecchi, F., Cavazza, D., Cicalò, C., Cifarelli, L., Coccetti, F., Coccia, E., Corvaglia, A., De Gruttola, D., De Pasquale, S., Galante, L., Garbini, M., . . . Zuyeuski, R. (2023). Measurement of the cosmic charged particle rate at sea level in the latitude range $35^\circ \div 82^\circ$ N with the PolarquEEEst experiment. European Physical Journal. C, Particles And Fields, 83(4). https://doi.org/10.1140/epjc/s10052-023-11353-w

[14] Köhli, M., Schrön, M., Zreda, M., Schmidt, U., Dietrich, P., & Zacharias, S. (2015). Footprint characteristics revised for field-scale soil moisture monitoring with cosmic-ray neutrons. Water Resources Research, 51(7), 5772–5790. https://doi.org/10.1002/2015wr017169

[15] Klages, H., Apel, W., Bekk, K., Bollmann, E., Bozdog, H., Brancus, I., Brendle, M., Chilingarian, A., Daumiller, K., Doll, P., Engler, J., Föller, M., Gabriel, P., Gils, H., Glasstetter, R., Haungs, A., Heck, D., Hörandel, J., Kampert, K., . . . Zeitnitz, B. (1997). The Kascade experiment. Nuclear Physics. B, Proceedings Supplement/Nuclear Physics. B, Proceedings Supplements, 52(3), 92–102. https://doi.org/10.1016/s0920-5632(96)00852-3

[16] Horneffer, A., Bähren, L., Buitink, S., Corstanje, A., Falcke, H., Hörandel, J., Lafebre, S., Scholten, O., Singh, K., Thoudam, S., & Ter Veen, S. (2010). Cosmic ray and neutrino measurements with LOFAR. Nuclear Instruments And Methods in Physics Research. Section A, Accelerators, Spectrometers, Detectors And Associated Equipment/Nuclear Instruments & Methods in Physics Research. Section A, Accelerators, Spectrometers, Detectors And Associated Equipment, 617(1–3), 482–483. https://doi.org/10.1016/j.nima.2009.10.092

[17] Abraham, J., Abreu, P., Aglietta, M., Aguirre, C., Ahn, E. J., Allard, D., Allekotte, I., Allen, J., Allison, P., Alvarez-Muiz, J., Ambrosio, M., Anchordoqui, L., Andringa, S., Anzalone, A., Aramo, C., Arganda, E., Argir, S., Arisaka, K., Arneodo, F., . . . Curutiu, A. (2010). The fluorescence detector of the Pierre Auger Observatory. Nuclear Instruments And Methods in Physics Research. Section A, Accelerators, Spectrometers, Detectors And Associated Equipment/Nuclear Instruments & Methods in Physics Research. Section A, Accelerators, Spectrometers, Detectors And Associated Equipment, 620(2–3), 227–251. https://doi.org/10.1016/j.nima.2010.04.023

[18] European Atlas of Natural Radiation | Chapter 8 - Cosmic radiation and cosmogenic radionuclides. (z.d.). In European Atlas Of Natural Radiation (pp. 158–160). https://remon.jrc.ec.europa.eu/media/351da5ac-63a2-4d45-a7e6-0ebe1fcd8e55/VQwvtw/Atlas/PDF%20Files/JRC_EANR_Chapter_08.pdf

[19] Ifedili, S. O. (1991). Atmospheric Neutrons and Their Contributions to the Earth's Radiation Belts. Journal Of Geomagnetism And Geoelectricity, 43(4), 255–266. https://doi.org/10.5636/jgg.43.255

[20] Dorman, L. I. (2004). Cosmic Rays in the Earth's Atmosphere and Underground. In Astrophysics and space science library. https://doi.org/10.1007/978-1-4020-2113-8

[21] Turekian, K., & Graustein, W. (2003). Natural Radionuclides in the Atmosphere. In Elsevier eBooks (pp. 261–279). https://doi.org/10.1016/b0-08-043751-6/04042-1

[22] Abdel Monem, A. A. & Nuclear Materials Authority. (z.d.). Comogenic Radionuclides in the Atmosphere: Origin and Applications. In XI Radiation Physics & Protection Conference. https://inis.iaea.org/collection/NCLCollectionStore/_Public/45/099/45099891.pdf?r=1

[23] Lal, D., & Peters, B. (1967). Cosmic Ray Produced Radioactivity on the Earth. In Handbuch der Physik (pp. 551–612).https://doi.org/10.1007/978-3-642-46079-1_7

[24] Gosse, J. C., & Phillips, F. M. (2001). Terrestrial in situ cosmogenic nuclides: theory and application. Quaternary Science Reviews, 20(14), 1475–1560. https://doi.org/10.1016/s0277-3791(00)00171-2

[25] Rall, W. (1956). The atomic nucleus. Robley Evans. McGraw Hill Book Company, Inc., New York (1955). 972 pp., $14.50. AIChE Journal, 2(3). https://doi.org/10.1002/aic.690020327

[26] Radioactiviteit in het leefmilieu | FANC - Federaal Agentschap voor Nucleaire Controle. (z.d.). https://fanc.fgov.be/nl/dossiers/radioactiviteit-het-leefmilieu

[27] Knoll, G. F. (2010). Radiation Detection and Measurement. John Wiley & Sons.

[28] Eljen Technology. EJ-426 - Thermal Neutron Detector - ElJeN Technology. https://eljentechnology.com/products/neutron-detectors/ej-426

[29] Eljen Technology.. EJ-200, EJ-204, EJ-208, EJ-212 - Plastic Scintillators - Eljen Technology. https://eljentechnology.com/products/plastic-scintillators/ej-200-ej-204-ej-208-ej-212

[30] Paepen, J., Schulte, F., Mastinu, P., Pedersen, B., Saare, H., Schillebeeckx, P., ... & Varasano, G. (2016). Characterisation of plastic scintillators used as an active background shield for neutron detection. JRC Tech Rep.

[31] Neutron Detection Screens and Imaging Screens | Scintacor. (2024, 15 mei). Scintacor. https://scintacor.com/products/neutron-detection-screens/

[32] SensL. (2011). An Introduction to the Silicon Photomultiplier. In Introduction To The SPM [Technical note]. https://www.seti.net/cosmic-rays/SETIPixel/CosmicWatch-Desktop-Muon-Detector-v2-master/Datasheets/Intro_to_SiPMs.pdf

[33] Wong, C., Hasan, W., & Isaak, S. (2015). The design and characterization of breakdown mechanism on p+/n- well single photon Avalanche Diode (Spad). https://www.semanticscholar.org/paper/The-design-and-characterization-of-breakdown-on-p%2B-Wong-Hasan/359029a14fe2bc9ebd418657de15bd3690615cd8

[34] Agostinelli, S., Allison, J., Amako, K., Apostolakis, J., Araujo, H., Arce, P., Asai, M., Axen, D., Banerjee, S., Barrand, G., Behner, F., Bellagamba, L., Boudreau, J., Broglia, L., Brunengo, A., Burkhardt, H., Chauvie, S., Chuma, J., Chytracek, R., . . . Zschiesche, D. (2003). Geant4—a simulation toolkit. Nuclear Instruments And Methods in Physics Research. Section A, Accelerators, Spectrometers, Detectors And Associated Equipment/Nuclear Instruments & Methods in Physics Research. Section A, Accelerators, Spectrometers, Detectors And Associated Equipment, 506(3), 250–303. https://doi.org/10.1016/s0168-9002(03)01368-8

[35] Uzhinsky, V. V. (2013, April). The Fritiof (FTF) model in GEANT4. In Proceedings, International Conference on Calorimetry for the High Energy Frontier (CHEF 2013): Paris, France (pp. 260-264).

[36] Wright, D. H., & Kelsey, M. H. (2015). The geant4 bertini cascade. Nuclear Instruments and Methods in Physics Research Section A: Accelerators, Spectrometers, Detectors and Associated Equipment, 804, 175-188.

[37] Koi, T., SLAC National accelerator Laboratory, CERN, IN2P3, IN2P3, & Geant4 electromagnetic working groups. (z.d.). EM Physics. In Geant4 v10.00.p01. https://www.slac.stanford.edu/xorg/geant4/SLACTutorial14/EMPhysics.pdf

[38] Geant4 Collaboration. (2020). Guide for Physics lists. In Guide For Physics Lists (Release 10.7). https://www.fe.infn.it/u/paterno/Geant4_tutorial/slides_further/guide/PhysicsListGuide.pdf

[39] Geant4 Collaboration. (2017). Physics Reference Manual. https://indico.cern.ch/event/679723/contributions/2792554/attachments/1559217/2454299/PhysicsReferenceManual.pdf

[40] Frass, W., Walczak, R., Michaelmas. (2009). C4: Particle Physics major option. https://www2.physics.ox.ac.uk/sites/default/files/Passage.pdf

[41] Freer, M., & Fynbo, H. o. u. (2014). The Hoyle state in 12C. Progress in Particle And Nuclear Physics, 78, 1–23. https://doi.org/10.1016/j.ppnp.2014.06.001

[42] Krammer, M., Erika Garutti, Kolanoski, Wermes, Kleinknecht, K., & Grupen, C. (z.d.). CALORIMETERS. In LECTURE 4 PART 4. https://indico.cern.ch/event/975141/contributions/4199689/attachments/2176109/3674649/2020-Lecture-4-4-Calorimeters.pdf

[43] Vesterinen, M. & University of Warwick. (z.d.). Calorimetry. https://indico.cern.ch/event/897634/contributions/3943446/attachments/2075809/3485586/WarwickWeek2020_Calorimeters.pdf

[44] Wingerter-Seez, I. (2018). Particle Physics instrumentation. arXiv (Cornell University). https://doi.org/10.48550/arxiv.1804.11246

[45] Abreu, Y., Giot, L., Pestel, V., Piñera, I., Mermans, J., Ryder, N., Boursette, D., Castle, B., Arnold, L., Simard, L., Lehaut, G., Koonen, E., Rademacker, J., De Roeck, A., Pronost, G., Guillon, B., Kalcheva, S., Janssen, X., Weber, A.,... Ghys, L. (2018). Performance of a full scale prototype detector at the BR2 reactor for the SoLid experiment. Journal Of Instrumentation, 13(05), P05005. https://doi.org/10.1088/1748-0221/13/05/p05005

[46] Abreu, Y., Amhis, Y., Beaumont, W., Bongrand, M., Boursette, D., Castle, B. C., Clark, K., Coupé, B., Cussans, D., De Roeck, A., Durand, D., Fallot, M., Ghys, L., Giot, L., Graves, K., Guillon, B., Henaff, D., Hosseini, B., Ihantola, S., ... Yermia, F. (2018). Optimisation of the scintillation light collection and uniformity for the SoLid experiment. Journal Of Instrumentation, 13(09), P09005. https://doi.org/10.1088/1748-0221/13/09/p09005

[47] Abreu, Y., Amhis, Y., Arnold, L., Barber, G., Beaumont, W., Binet, S., Bolognino, I., Bongrand, M., Borg, J., Boursette, D., Buridon, V., Castle, B., Chanal, H., Clark, K., Coupé, B., Crochet, P., Cussans, D., De Roeck, A., Durand, D., . . . Yermia, F. (2021). SoLid: a short baseline reactor neutrino experiment. Journal Of Instrumentation, 16(02), P02025. https://doi.org/10.1088/1748-0221/16/02/p02025

[48] Vercaemer, S. (2016). Neutron identification in the SoLid experiment. Proceedings Of The European Physical Society Conference On High Energy Physics — PoS(EPS-HEP2015). https://doi.org/10.22323/1.234.0083

Appendix: SoLi∂

The Standard Model of Particle Physics of particle physics is a beautiful theory that has helped us understand the world for many years. Unfortunately, this theory does not give us all the answers. Many questions still remain unanswered. Hints toward Beyond Standard Model Physics (BSM) are intensively sought.
One of the experiments that was set up to investigate an experimental anomaly is the SoLi∂ experiment [45],[46],[47],[48]. The Search for oscillation with Lithium-6 detector, or short SoLi∂ experiment, searches for sterile neutrinos via neutrino oscillations. Sterile neutrinos are just like the Standard Model neutrinos, they do not carry any electric or color charge, but additionally, they do not interact via the weak interaction either. This means they do not carry any charge from any force. Since they are free from influences from Standard Model forces, sterile neutrinos are hard to detect. However, just like Standard Model neutrinos, it could be possible that sterile neutrinos participate in neutrino flavor-changing oscillations. So by investigating sources of neutrinos, it could be possible to study them[45].
The SoLi∂ experiment is set up at the BR2 research reactor at the SCK·CEN in Mol, Belgium. The reactor provides the experimental setup with a neutrino source. The neutrino oscillations are then investigated between 6 and 9 meters from the reactor. Since sterile neutrinos are impossible to detect directly, their measurement principle is based on the identification of inverse beta decay products. Inverse beta decay (IBD) happens when an electron antineutrino interacts with a proton inside the detector. This results in a positron and a neutron.

$$\bar{\nu}_e + p \rightarrow e^+ + n$$

The positron and neutron are then detected by the experimental setup, which consists of scintillator cubes provided with a $^6LiF : ZnS(Ag)$ screen, wrapped in Tyvek shells. The scintillator cubes have a dimension of 5 cm $\times$ 5 cm $\times$ 5 cm and are stacked in planes of 16 $\times$ 16 cubes. Five modules of 10 planes are then placed near the reactor. Wavelength-shifting fibers (WSl) guide the light of the scintillator cubes toward the Silicon Photon Multipliers (SiPM). Here the light gets collected and converted into an electric signal.

The SoLi∂ experiment is interested in the neutrino sector, which means that all other particles are considered as background. Even though the SoLi∂ experiment has access

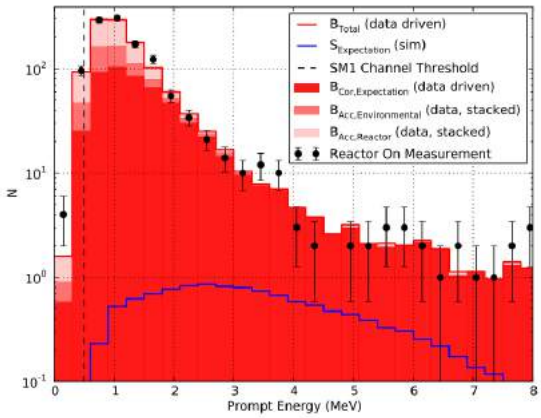

Figure 6.1: Prompt energy distribution for reactor-on data. The predicted background is shown in red (stacked). The small predicted neutrino contribution is shown in blue. Note that the prototype detector trigger threshold was set $\sim$500 keV.

to a high flux neutrino source, a challenge for the experiment lies in cosmic-ray background radiation. This can be seen in figure 6.1. The cosmic ray background consists mainly of atmospheric muons, neutrons and hadrons that interact with the detector. A fast neutron signal could be created in some of these interactions. They look similar to time-correlated inverse beta decay events. Fast neutrons are either part of the incoming cosmic ray flux or by-products from spallation reactions induced by muons interacting with the detector and surrounding material. The slow neutrons contribute to the accidental background when a slow neutron and a gamma ray are accidentally detected within the time window that is used from the search for inverse beta decay signals.

As the components of this experiment retired, they are recycled in this thesis. The focus of the thesis lies where SoLi∂ has its background. The goal is to explore the possibilities with these interesting components.